

Optical and Photocatalytic Properties of Three-Dimensionally Ordered Macroporous Ta₂O₅ and Ta₃N₅ Inverse Opals

Yusong Dong, Fujisaka Ai, Dongxiao Sun-Waterhouse, Kei-ichiro Murai, Toshihiro Moriga, and Geoffrey I. N. Waterhouse*



Cite This: *Chem. Mater.* 2023, 35, 8281–8300



Read Online

ACCESS |



Metrics & More

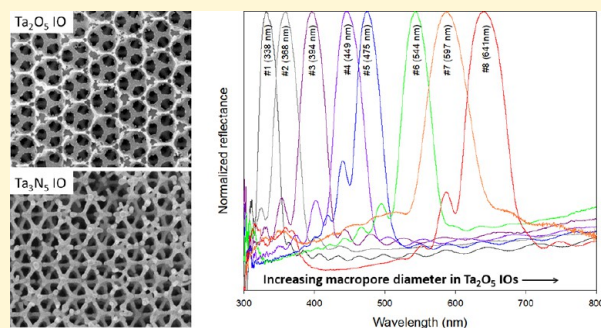


Article Recommendations



Supporting Information

ABSTRACT: Colloidal crystal templating is a simple yet remarkably versatile synthetic strategy toward inverse opal (IO) photonic crystals for optical sensing and catalytic applications. Herein, we report the successful fabrication of tantalum (V) oxide, Ta₂O₅, inverse opal thin films and powders using the colloidal crystal templating method, utilizing poly(methyl methacrylate) (PMMA) colloidal crystals as sacrificial templates and TaCl₅ as the tantalum source. The Ta₂O₅ IO thin films and powders showed structural color at ultraviolet (UV) and visible wavelengths, with the photonic band gap (PBG) position along the [111] direction increasing linearly with the diameter of macropores (*D*) in the inverse opals and also the refractive index of the medium filling the macropores, in excellent accord with a modified Bragg's law expression. Thermal ammonolysis of the Ta₂O₅ inverse opals at 700 °C yielded well-ordered Ta₃N₅ IO films and powders possessing high specific surface areas (37 m² g⁻¹) and a semiconductor band gap of 2.0–2.1 eV. A Pt/Ta₃N₅ IO photocatalyst delivered a H₂ production rate of ~300 μmol g⁻¹ h⁻¹ in aqueous methanol (10 vol % MeOH) under visible-light irradiation (300 W Xe lamp, λ ≥ 420 nm), approximately twice that achieved using conventional Pt/Ta₃N₅ powder photocatalysts (161 μmol g⁻¹ h⁻¹, 8.4 m² g⁻¹). Results demonstrate that inverse opal engineering is an effective approach for realizing Ta₂O₅ IO thin films for sensing applications and Ta₃N₅ IOs with enhanced photocatalyst performance.



INTRODUCTION

With a view toward the fabrication of well-ordered porous oxide materials for sensors and catalytic applications, researchers are increasingly utilizing colloidal crystal templating strategies. This approach involves the self-assembly of monodisperse spherical colloids, typically submicron-sized polystyrene or poly(methyl methacrylate) colloids, on a face-centered cubic (fcc) lattice to form a colloidal crystal (synthetic opal).^{1–11} Subsequently, the interstitial voids in the colloidal crystal templates are filled with a dielectric material via sol–gel, electrodeposition, chemical vapor deposition (CVD), atomic layer deposition (ALD), precipitation, or nanoparticle infiltration methods, followed by selective removal of the polymer colloidal crystal template via calcination or solvent etching.^{1–11} The product, commonly referred to as an inverse opal (IO), comprises a face-centered cubic array of uniformly sized air spheres (macropores) in a dielectric matrix. Using this approach, a diverse array of three-dimensionally ordered (3DOM) metal oxide inverse opals (e.g., SiO₂, TiO₂, ZrO₂, Al₂O₃, and CeO₂) and other kinds of inverse opals (including conducting polymers, metals, etc.) have been fabricated.^{1–16} The periodically modulated refractive index that naturally exists in opal and inverse opal arrays creates photonic band gaps (PBGs) or optical stop bands along particular directions in the fcc lattice.^{17–19} If the periodicity (*d*_{hkl}) in metal

oxide inverse opals is around half that of visible-light wavelengths (i.e., *d*_{hkl} = 200–375 nm), angle-dependent structural color in the visible region is typically observed, thus providing a basis for optical sensor development (since the PBG position, λ_{max}, and hence the reflected color are sensitive to the refractive index of the medium filling the macropores). For first-order diffraction on fcc planes in opal and inverse opal photonic crystals, PBG positions can be described using the following modified Bragg's law expression:

$$\lambda_{\max} = 2d_{hkl} \sqrt{n_{\text{avg}}^2 - \sin^2 \theta} \quad (1)$$

where λ_{max} is the PBG position (in nm), *d*_{hkl} is the interplanar spacing between *hkl* planes (in nm), θ is the incident angle of light with respect to the surface normal (in degrees), and *n*_{avg} is the average refractive index of the opal or inverse opal. The latter can be calculated using the equation:

Received: July 31, 2023

Revised: August 30, 2023

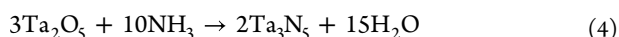
Published: September 21, 2023



$$n_{\text{avg}} = [\phi_{\text{solid}} n_{\text{solid}} + (1 - \phi_{\text{solid}}) n_{\text{void}}] \quad (2)$$

where ϕ_{solid} is the solid volume fraction in the opal or inverse opal (typically 0.74 for an opal, <0.26 for an inverse opal), n_{solid} is the refractive index of the solid material, and n_{void} is the refractive index of the void filling material.²

Tantalum pentoxide (Ta_2O_5) is an important metal oxide, possessing a high refractive index (2.05–2.3) and high transparency in both the visible and near-infrared regions. These properties make it a particularly attractive material for creating optical and optoelectronic devices, including sensors, filters, lasers, and photographic lenses.^{20–27} Further, the combination of a high dielectric constant ($\epsilon = 29$, increasing to 90–110 in thin films) and wide electronic band gap ($E_g = 4.0$) lead to further application in capacitors and other electronic devices. Surprisingly, given the excellent optical properties of Ta_2O_5 , very little work has been reported to date relating to the fabrication of Ta_2O_5 inverse opals operating in the visible regime.^{27–29} The 3DOM structure of inverse opals, together with their inherent photonic crystal properties, is expected to create new opportunities for Ta_2O_5 in optical sensor development,^{30–37} photocatalysis,^{37–44} and catalysis,^{37,38,45–49} motivating a detailed investigation. Furthermore, Ta_2O_5 is an important starting material in the preparation of TaON and Ta_3N_5 photocatalysts for visible-light-driven hydrogen production. Olive green TaON ($E_g = 2.4\text{--}2.5$ eV) is typically obtained by nitridation of Ta_2O_5 at 800–950 °C and low NH_3 flow rates (25–50 mL min^{-1}), whereas orange-red Ta_3N_5 ($E_g = 2.0\text{--}2.1$ eV) is generated at lower temperatures (~ 700 °C) and high ammonia flow rates (0.5–1 L min^{-1}). The syntheses of TaON and Ta_3N_5 are described by the following equations:



The TaON and Ta_3N_5 products produced using commercial Ta_2O_5 powders or sol–gel-derived Ta_2O_5 powders generally have low specific surface areas (generally <10 $\text{m}^2 \text{g}^{-1}$) due to the high reaction temperatures used in their synthesis. This limits their photocatalytic activities. We hypothesized that by using an inverse opal Ta_2O_5 IO precursor, particle sintering during the thermal nitridation to produce TaON or Ta_3N_5 should be greatly suppressed (since particle sintering cannot easily occur across the large inverse opal macropores), thus producing visible-light-driven photocatalysts with high specific surface areas and improved photocatalytic activity. Validation of this hypothesis is one focus of this manuscript.

In this work, we report a detailed investigation of Ta_2O_5 inverse opal fabrication using the colloidal crystal template method. Using PMMA colloidal crystals as sacrificial templates, we demonstrate that high-quality Ta_2O_5 inverse opal thin films with pseudo PBGs along [111] at UV and visible wavelengths can readily be prepared for optical sensing applications. This fills a critical gap in the scientific literature, since almost all previously reported optical data for Ta_2O_5 IOs are for polycrystalline powders, not thin films (with oriented thin films being desirable for optical sensing applications). Further, we also demonstrate that the thermal ammonolysis of Ta_2O_5 IO films and powders at 700 °C yields phase-pure Ta_3N_5 IOs with high specific surface areas and excellent photocatalytic activities for hydrogen production under visible light. Results encourage the wider use of colloidal crystal templating to enhance the functionality of transition metal oxide and nitride materials.

EXPERIMENTAL METHODS

Materials. Methyl methacrylate (MMA, 99%), 2,2'-azobis(2-methylpropionamide)dihydrochloride (97%), tantalum(V) chloride (TaCl_5 , 99.99%), concentrated HCl (37 wt % in water), and chloroplatinic acid hexahydrate ($\text{H}_2\text{PtCl}_6 \cdot 6\text{H}_2\text{O}$, 98%) were purchased from Sigma-Aldrich and used without further purification. Methanol (99%), acetone (99%), ethanol (99.4%), *n*-heptane (99.5%), dichloromethane (DCM, 99%), carbon tetrachloride (CCl_4 , 99.5%), and toluene (98%) were obtained from local suppliers. Water was obtained from a Milli-Q system (18.2 $\text{M}\Omega\text{-cm}$).

Synthesis of Monodisperse Poly(methyl methacrylate) Colloids. Eight batches of monodisperse PMMA colloids with different diameters were synthesized by the surfactant-free emulsion polymerization of methyl methacrylate at 70–85 °C (Table 1), following the general procedure described by Schroden et al., with some modifications.⁵⁰ The polymerizations were conducted in a five-neck round-bottom flask fitted with a mechanical stirrer, water-cooled condenser, thermometer, nitrogen gas flow inlet tube, and a glass stopper (Figure S1). By varying the reaction temperature and the volume of MMA added, eight batches of monodisperse PMMA colloids with diameters ranging from 224 to 414 nm were obtained.

Table 1. Synthesis Parameters Used to Prepare the Eight Batches of Monodisperse Poly(methyl methacrylate) Colloids

| batch | temp. (°C) | volume MMA (mL) | volume H_2O (L) | mass azo initiator (g) | D_{SEM} (nm) |
|-------|------------|-----------------|---------------------------------|------------------------|-----------------------|
| #1 | 85 | 125 | 1.6 | 1.5 | 224 |
| #2 | 85 | 150 | 1.6 | 1.5 | 235 |
| #3 | 80 | 175 | 1.6 | 1.5 | 261 |
| #4 | 80 | 200 | 1.6 | 1.5 | 294 |
| #5 | 80 | 300 | 1.6 | 1.5 | 320 |
| #6 | 70 | 300 | 1.6 | 1.5 | 360 |
| #7 | 70 | 350 | 1.6 | 1.5 | 390 |
| #8 | 70 | 400 | 1.6 | 1.5 | 414 |

Fabrication of Poly(methyl methacrylate) Colloidal Crystals (PMMA CCs). PMMA colloidal crystal thin films on glass or quartz microscope slides and free-standing monoliths were subsequently prepared from each batch of PMMA colloids. These templates were used to fabricate Ta_2O_5 IO thin films and Ta_2O_5 IO powders, respectively. The flow-controlled vertical deposition method (FCVD) method was used to deposit PMMA CC thin films on glass or quartz microscope glass slides (2 cm × 5 cm) for optical characterization studies (Figure S2).⁵¹ Free-standing PMMA monoliths were prepared by centrifugation. Conical polypropylene centrifuge tubes (50 mL) were filled with the undiluted PMMA colloidal dispersions. The tubes were then centrifuged at 1500 rpm (rcf 369) for 24 h at room temperature using an Eppendorf 5804 centrifuge. Following centrifugation, the supernatant was carefully removed using a plastic pipette, and the centrifuge tubes containing the colloidal crystal pellets were then left to stand vertically (uncovered) at room temperature in a fume hood for 3 weeks until completely dry. The obtained PMMA colloidal crystal monoliths were then used to fabricate Ta_2O_5 IO powders.

Fabrication of Ta_2O_5 Inverse Opals (Ta_2O_5 IOs) by Colloidal Crystal Templating. For the preparation of the Ta_2O_5 IO films, a 5 wt % TaCl_5 solution in ethanol was prepared. For the fabrication of the Ta_2O_5 IO powders using the PMMA CC monoliths, a 10 wt % TaCl_5 solution in ethanol was used.

To infiltrate the PMMA CC films on glass or quartz microscope slides, one end of each slide was slightly elevated to give a tilt angle of $\sim 5^\circ$ between the high and low ends of the slide. Then, 4 drops of the ethanolic 5 wt % TaCl_5 solution were applied on the raised edge of the PMMA colloidal crystal films. The combination of gravity and capillary action resulted in the complete filling of the voids in the colloidal crystal

films. After infiltration, the slides were laid flat (film side upward) and allowed to dry in air for 24 h.

For the preparation of Ta₂O₅ IO powders, the centrifuged PMMA colloidal crystal monoliths were lightly crushed with a spatula to give small pieces of size 1–2 mm. The pieces of colloidal crystal were then spread as a thin layer on a piece of ethanol-moistened Whatman grade 2 filter paper in a Büchner funnel, with a strong vacuum applied. The 10 wt % TaCl₅ solution (in ethanol) was then applied dropwise over the layer of the PMMA colloidal crystal pieces until all pieces had been wetted. A strong vacuum was applied for a further 15 min to remove any excess TaCl₅ solution. Finally, the infiltrated PMMA CC pieces were allowed to dry in air for 24–48 h at room temperature.

The sol–gel infiltrated PMMA CCs were then transformed into Ta₂O₅ IOs by calcination. Briefly, the samples were heated from room temperature to 300 °C in air at 2 °C min⁻¹ and then held at 300 °C for 2 h; then, the temperature was increased from 300 to 550 °C at 2 °C min⁻¹ and held at 550 °C for 2 h (for films) or 4 h (for powders). The samples were then removed from the furnace at 550 °C and allowed to cool to room temperature in air. The resulting Ta₂O₅ inverse opal films and powders showed “opalescence” under white light and were subjected to detailed optical and structural characterization studies.

Fabrication of Ta₃N₅ Inverse Opals (Ta₃N₅ IOs) by Thermal Ammonolysis. Ta₃N₅ IOs were synthesized by thermal ammonolysis of the Ta₂O₅ IO films (on quartz) and powders at 700 °C for 5 h under an ammonia gas flow. The nitridations were conducted in an alumina tube reactor (housed in a tube furnace) that was sealed at one end and fitted with ammonia inlet/gas outlet tubes at the other end (Figure S3). At the beginning of the experiments, Ta₂O₅ IO samples were placed in alumina boats and then transferred to the reactor. Samples were heated from room temperature to 550 °C at ~8 °C min⁻¹ under helium gas, and then the gas switched to pure NH₃ gas (1 L min⁻¹, 99.99%). The samples were then heated to 700 °C at 1 °C min⁻¹ and then held at 700 °C for 5 h. The samples were then allowed to cool naturally in the alumina tube reactor, with the gas switched from NH₃ to He once the temperature had dropped below 500 °C. Once the temperature of the furnace was below 100 °C, the nitrided samples were collected for characterization.

Characterization. Scanning electron microscopy (SEM) images were collected on a Philips XL-30S Field Emission Gun scanning electron microscope (FEGSEM) operating at an electron accelerating voltage of 5 kV in high vacuum. Samples were mounted on black carbon tape for the analyses and then lightly platinum sputter coated (Quorum Q150RS) to reduce specimen charging under the electron beam.

Transmission electron microscopy (TEM) analyses used a Tecnai 12 transmission electron microscope operated at an accelerating voltage of 120 kV. An under-mounted GATAN CCD 4-megapixel camera was used to collect the images. Powder specimens were dispersed in ethanol, and then a drop of the dispersion was placed on a 400 mesh copper viewing grid. After evaporation of the ethanol, the samples were transferred into the vacuum system of the TEM instrument for imaging.

UV–vis transmittance spectra for the PMMA CC films, Ta₂O₅ IO films, and Ta₃N₅ IO films were recorded over the wavelength range 300–1100 nm on a Shimadzu UV-1700 spectrometer. The sample compartment of the instrument contained a customized sample holder for UV–vis transmittance measurements at different incident angles with respect to the surface normal of the films. For studies examining the optical properties of the inverse opal films in different organic solvents, the angle measurement holder was replaced by a standard quartz cuvette holder (path length 10 mm). Solvents used were methanol, acetone, ethanol, *n*-heptane, DCM, CCl₄, and benzene.

UV–vis reflectance spectra from the PMMA CC films, Ta₂O₅ IO films, and Ta₃N₅ IO films were acquired on an Ocean Optics CD S-2000 spectrometer connected to a bifurcated fiber optic cable coupled to a microscope objective lens. The light source was an Ocean Optics DH-2000-BAL with deuterium and halogen light sources. Light from the source was focused to a spot size of 1 mm², with the illumination occurring along the surface normal of the photonic crystal thin films (i.e., along [111] direction). The reflected light was also collected along the surface normal (i.e., using a 180° backscattering geometry). Spectra

were collected over the wavelength range 300–880 nm with a spectral acquisition time of 100 ms and boxcar smoothing of 2 nm.

N₂ physisorption isotherms for the inverse opal powders were determined on a Micromeritics Tristar 3000 instrument at liquid nitrogen temperature (77 K). Specific surface areas were calculated from the N₂ physisorption data according to the Brunauer–Emmett–Teller (BET) method using P/P_0 values in the range of 0.05–0.1.⁵² Cumulative pore volumes and average pore diameters were calculated from the adsorption isotherms by the Barrett–Joyner–Halenda (BJH) method.⁵³ Prior to analysis, samples were heated at 80 °C overnight in a vacuum oven.

Powder X-ray diffraction (XRD) patterns were collected on a PANalytical Empyrean powder X-ray diffractometer equipped with a Cu anode X-ray tube and a curved graphite filter monochromator. Measurements were performed from $2\theta = 5$ –90° (step 0.02°, scan rate 2° min⁻¹) using monochromated Cu K α_1 radiation (wavelength 1.5418 Å, current 40 mA, voltage 40 kV) at room temperature.⁵⁴

X-ray photoelectron spectroscopy (XPS) data were obtained on Kratos Axis UltraDL equipped with a hemispherical electron energy analyzer, analysis chamber of base pressure $\sim 1 \times 10^{-9}$ Torr, and an Al K α X-ray source (1486.6 eV). A charge neutralization system was used to minimize sample charging during analysis. Survey scans were obtained at a hemispherical analyzer pass energy of 160 eV over the binding energy range of 1300 to –5 eV, while core-level scans over the Ta 4f, O 1s, N 1s, and Pt 4f regions used an analyzer pass energy of 20 eV.

The oxygen and nitrogen contents in the Ta₂O₅ IO and Ta₃N₅ IO samples were determined by the hot gas extraction method using a Horiba EMGA-920 analyzer (O/N analyzer). In the O/N analyses, the samples were rapidly heated in a graphite crucible. The oxygen in the sample was converted to carbon monoxide and carbon dioxide and quantified using a nondispersive infrared detector, while the nitrogen in the sample was converted to N₂ and measured using a thermal conductivity detector.

Photonic Band Structure Simulations. Photonic band-gap structure diagrams for the PMMA colloidal crystals and Ta₂O₅ inverse opal were created using a freely available software package, “MIT photonic band.” Fully vectorial eigenmodes of Maxwell’s equations with periodic boundary conditions were computed by preconditioned conjugate-gradient minimization of the block Rayleigh quotient in a plane-wave basis, along the high symmetry directions U–L–Γ–X–W–K of the 3D face-centered cubic 1st Brillouin zone.⁵⁵

Photocatalytic Hydrogen Production Tests. The photocatalytic H₂ production tests were performed in a tubular Pyrex glass reactor (105 mL volume). Ta₃N₅ IOs (10 mg) were dispersed in 20 mL of a 10 vol % methanol solution (2 mL of methanol; 18 mL of deionized water) containing a certain amount of H₂PtCl₆·6H₂O. Prior to photoirradiation, the stirred reaction suspension was kept under an N₂ flow for 20 min to completely remove any dissolved oxygen. The reactor was then sealed, and the suspension was irradiated by a xenon lamp (300 W, Beijing Perfectlight Co., Ltd.) fitted with a 420 nm cutoff filter ($\lambda \geq 420$ nm) (Figure S4). To avoid excessive heating of the reactor under the Xe lamp, cold air was blown directly onto the reactor to keep the temperature at ~30 °C. At regular intervals, 1 mL samples of the headspace gas were collected and injected into a Shimadzu GC 2014 equipped with a Carboxen-1010 plot capillary column and thermal conductivity (TCD) detector. H₂ evolved was quantified using an external calibration curve. Photocatalytic tests for each sample were carried out in triplicate, with data expressed as mean \pm standard deviation.

RESULTS AND DISCUSSION

Structural Characterization of PMMA Colloidal Crystal Films and Ta₂O₅ IO Replicas. Eight batches of monodisperse PMMA colloids were prepared by the surfactant-free emulsion polymerization of methyl methacrylate (MMA) at temperatures between 70–85 °C. Table 1 shows the effect of polymerization conditions (temperature and the volume of MMA) on the size of PMMA colloids. Increasing the temperature at a fixed volume of

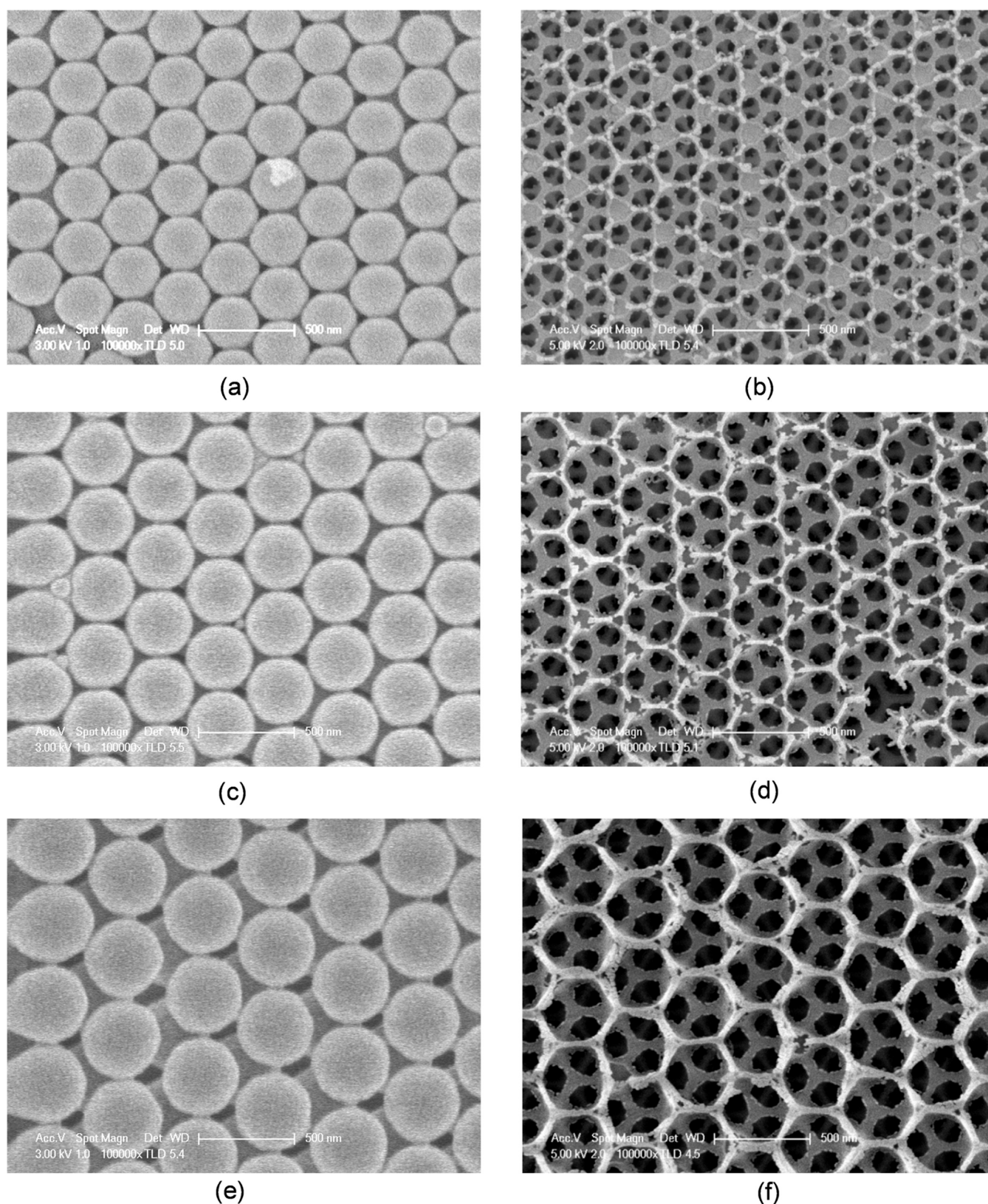


Figure 1. SEM images of selected PMMA colloidal crystal films and their corresponding Ta_2O_5 inverse opal replicas viewed along the $[111]$ direction. (a) #4 PMMA CC, (b) #4 Ta_2O_5 IO, (c) #6 PMMA CC, (d) #6 Ta_2O_5 IO, (e) #8 PMMA CC, and (f) #8 Ta_2O_5 IO. All images were taken at a magnification of 100,000 \times ; scale bar 500 nm.

MMA or decreasing the volume of MMA at a fixed temperature resulted in smaller PMMA colloids. Through manipulating these

two parameters, eight batches of monodisperse PMMA colloids with diameters between 224 and 414 nm were obtained.

Table 2. Summarized Structural and Optical Properties of the PMMA Colloidal Crystal Films

| batch | D_{SEM} (nm) | PBG [111] (nm) | $D_{\theta=0^\circ}$ (nm) ^a | $\Delta\lambda/\lambda_{\text{max}}$ | a/λ_{max} | D_{angle} (nm) ^b | n_{avg} ^b | ϕ_{PMMA} ^b |
|-------|-----------------------|----------------|--|--------------------------------------|--------------------------|--------------------------------------|-------------------------------|-----------------------------------|
| #1 | 224 | 498 | 223.6 | 0.076 | 0.636 | 209.5 | 1.453 | 0.768 |
| #2 | 235 | 525 | 235.7 | 0.073 | 0.633 | 213.0 | 1.505 | 0.656 |
| #3 | 261 | 583 | 261.7 | 0.076 | 0.633 | 248.7 | 1.435 | 0.738 |
| #4 | 294 | 655 | 294.1 | 0.076 | 0.635 | 288.5 | 1.392 | 0.664 |
| #5 | 320 | 714 | 320.7 | 0.072 | 0.634 | 321.4 | 1.321 | 0.545 |
| #6 | 360 | 803 | 360.5 | 0.075 | 0.634 | 350.7 | 1.402 | 0.682 |
| #7 | 390 | 868 | 389.7 | 0.077 | 0.635 | 379.0 | 1.404 | 0.685 |
| #8 | 414 | 920 | 413.0 | 0.083 | 0.636 | 414.4 | 1.368 | 0.695 |

^aCalculated from the PBG, assuming a solid volume fraction of 0.74 and $n_{\text{PMMA}} = 1.492$. ^bCalculated from plots of λ_{max}^2 vs $\sin^2 \theta$.

The high monodispersity of each colloid batch meant that the well-ordered colloidal crystals could easily be prepared using the FCVD or centrifugation methods described in the experimental section. Figure 1a,c,e shows SEM images for PMMA colloidal crystal films prepared using batches #4, #6, and #8 PMMA colloids. The films crystallized with fcc (111) planes parallel to the underlying glass/quartz microscope slides. The diameter (D) of the PMMA colloidal crystals measured from the SEM images were 294, 360, and 414 nm, respectively (Tables 1 and 2).

Figure 2a,c,e shows cross sections of the PMMA CC films, showing good adherence to the underlying substrates, with film thicknesses ranging from 3–5 μm (film thicknesses could be controlled to some extent by changing the PMMA colloid concentration and also the peristaltic pump speed). Owing to their excellent 3D order, the PMMA colloidal crystal films served as excellent sacrificial templates for the synthesis of high-quality Ta_2O_5 inverse opal films.

Figure 1b,d,f shows SEM images for Ta_2O_5 inverse opal films prepared using the #4, #6, and #8 PMMA colloidal crystal films. The small windows in the macropores show areas where PMMA colloids “necked” in the templates and thus could not be infiltrated by the TaCl_5 solution. The macropore diameters (D) in the samples were 258, 315, and 350 nm, respectively (see Table 3 below), approximately 15% smaller than the corresponding D values for the PMMA colloidal crystal templates (Table 2). Approximately the same degree of shrinkage was observed in all eight batches of Ta_2O_5 IOs, with the shrinkage originating from densification of the Ta_2O_5 network following PMMA template removal at high temperatures. A plot of $D_{\text{Ta}_2\text{O}_5}$ vs D_{PMMA} yielded a straight line with a slope of 0.85 (Figure S5), showing the close relationship between the structural properties of the inverse opals and their corresponding PMMA templates. The decrease in the D value on going from the PMMA colloidal crystals to Ta_2O_5 inverse opal replicas caused cracking of the films, with the inverse opal films consisting of large islands of well-ordered inverse opal (lateral size $\sim 50 \mu\text{m}^2$) with gaps in between. Despite the cracking of the films, the Ta_2O_5 IOs domains maintained good local order and adhesion with the underlying substrates (as seen in the cross-sectional images in Figure 2b,d,f), with their (111) planes parallel to the substrate. Accordingly, the Ta_2O_5 IO films possessed adequate structural uniformity to create pseudo photonic band gaps at UV and visible wavelengths, allowing their application in optical sensing and the fabrication of Ta_3N_5 IOs, as explored in detail below.

Figure 3a,b shows TEM images for a piece of the #6 Ta_2O_5 IO film. The sample was prepared for analysis by carefully scraping the Ta_2O_5 IO film from its underlying glass microscope slide with a razor blade. No crystallites could be seen in the walls of

the Ta_2O_5 IOs prepared at 550 $^\circ\text{C}$, suggesting an amorphous oxide phase. This was confirmed by XRD (Figure 3c), with the as-prepared Ta_2O_5 IOs powders showing only a few broad features.^{56,57} However, calcination of the Ta_2O_5 IOs at higher temperatures resulted in crystallization of the Ta_2O_5 network, resulting in the appearance of sharp peaks due to orthorhombic Ta_2O_5 ($Pmm2$, with lattice constants of $a = 43.997 \text{ \AA}$, $b = 3.894 \text{ \AA}$, and $c = 6.209 \text{ \AA}$), as shown in Figure 3d. For the purpose of this study, we focus simply on the Ta_2O_5 IO samples prepared by calcination at 550 $^\circ\text{C}$ since those samples offered the best structural color.

Optical Characterization of the PMMA Colloidal Crystal Films and Ta_2O_5 IO Replicas. The optical properties of the PMMA colloidal crystal films were studied by UV–vis reflectance and transmittance spectroscopy. Data for the eight batches of PMMA colloidal crystal films are shown in Figure S6. The #1 to #8 PMMA CC films showed photonic band gaps (PBGs) along the [111] direction (i.e., perpendicular to the films) at 498, 525, 583, 655, 714, 803, 868, and 920 nm, respectively, in air. The PBGs appear as maxima in the reflectance spectra and minima in the transmittance spectra. On either side of the PBG along the [111] direction, the films showed good optical transparency. The [111] PBG for the #8 PMMA CC film was outside the range of the reflectance spectrometer used in this work. For first-order Bragg diffraction on fcc (111) planes of colloidal crystals of inverse opals, eq 1 transforms to give the following equation:

$$\lambda_{\text{max}} = 1.633D\sqrt{n_{\text{avg}}^2 - \sin^2 \theta} \quad (5)$$

where λ_{max} is the PBG position along the [111] direction, θ is the angle of light with respect to the surface normal of the (111) planes (i.e., angle with respect to the [111] direction), and n_{avg} is the average refractive index of the photonic crystals. For PMMA colloidal crystals in air with an ideal solid volume fraction of 0.74, $n_{\text{avg}} = (0.74 \times 1.492 + 0.26 \times 1.00) = 1.364$, based on $n_{\text{PMMA}} = 1.492$ and $n_{\text{air}} = 1.00$. For a colloidal crystal or inverse opal in air and $\theta = 0^\circ$, eq 5 further simplifies to give

$$\lambda_{\text{max}} = 1.633Dn_{\text{avg}} \quad (6)$$

Substituting $n_{\text{avg}} = 1.364$ into eq 6 gives $\lambda_{\text{max}} = 2.227D$ for a PMMA colloidal crystal in air. Hence, the position of PBGs along the [111] direction is directly proportional to the PMMA colloid diameter (D), which agrees perfectly with the red shift seen in the PBG positions of the PMMA colloidal crystals on going from #1 PMMA CC to #8 PMMA CC (Figure S6a,b and Table 2). Equation 5 also predicts that PBG along the [111] direction will blue-shift as the incident angle of light (θ) with respect to the [111] direction increases, in excellent accord with the experimental UV–vis transmittance data shown in Figure

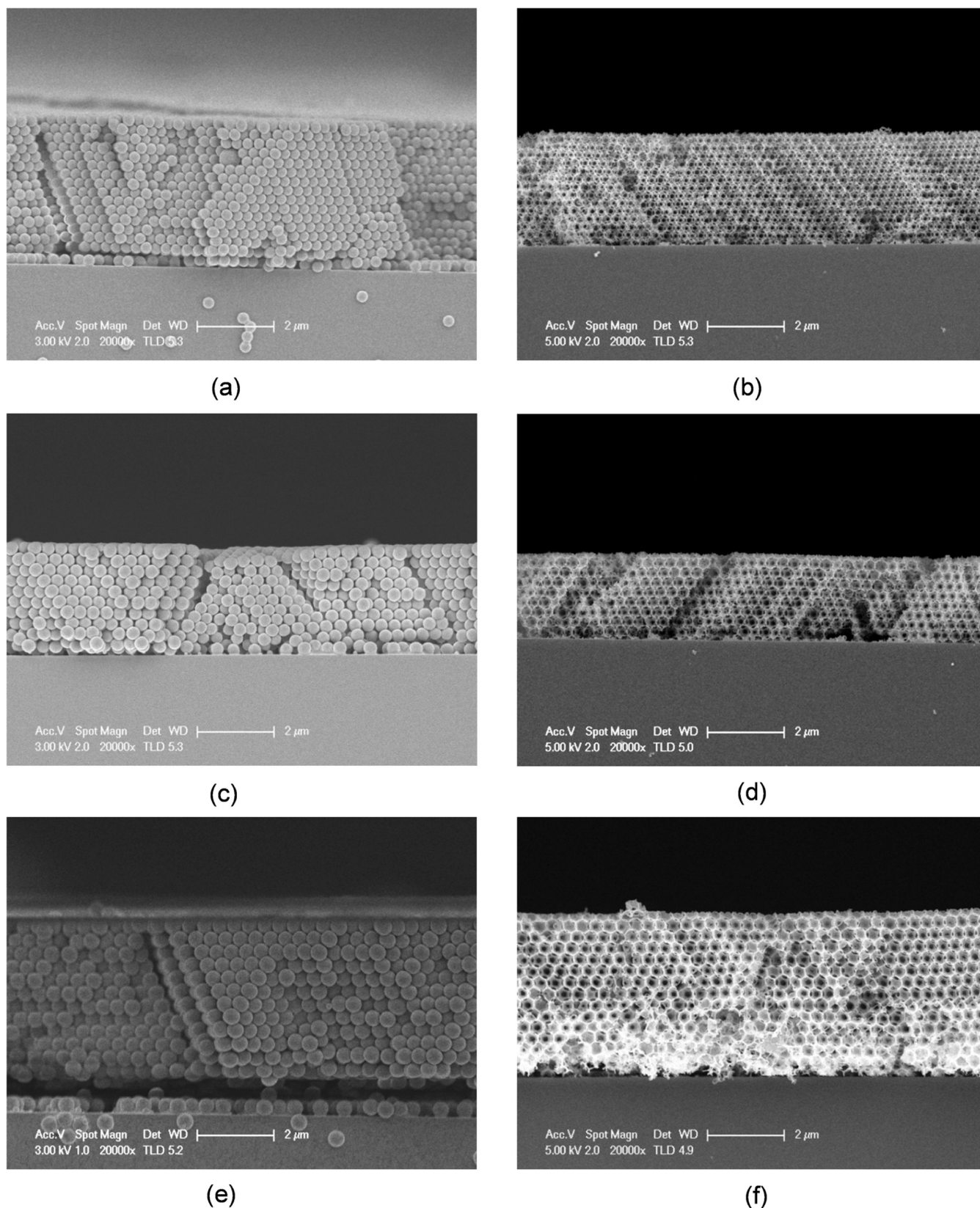


Figure 2. Cross-sectional SEM images of selected PMMA colloidal crystal films and their corresponding Ta₂O₅ inverse opals replicas. (a) #4 PMMA CC, (b) #4 Ta₂O₅ IO, (c) #6 PMMA CC, (d) #6 Ta₂O₅ IO, (e) #8 PMMA CC, and (f) #8 Ta₂O₅ IO. Images were taken at a magnification of 20,000 \times ; scale bar 2 μ m.

S6c–e. By taking the square of both sides of eq 5, a linear relationship is predicted between λ_{\max}^2 and $\sin^2 \theta$, which was

confirmed in Figure S6f using the data shown in Figure S6c–e. The slopes ($-1.633^2 D^2$) and the y -axis intercepts

Table 3. Summarized Structural and Optical Properties of the Ta₂O₅ Inverse Opals

| batch | <i>D</i> _{SEM} (nm) | PBG [111] (nm) | <i>D</i> _{θ=0°} (nm) ^a | Δ <i>λ</i> / <i>λ</i> _{max} | <i>a</i> / <i>λ</i> _{max} | <i>D</i> _{angle} (nm) ^b | <i>n</i> _{avg} ^b | <i>D</i> _{solvent} (nm) ^c | <i>n</i> _{avg} ^c | φ _{Ta₂O₅} ^c |
|-------|------------------------------|----------------|--|--------------------------------------|------------------------------------|---|--------------------------------------|---|--------------------------------------|---|
| #1 | 184 | 338 | 188.2 | 0.090 | 0.770 | | | 194.7 | 1.036 | 0.032 |
| #2 | 200 | 368 | 204.9 | 0.102 | 0.769 | | | 202.8 | 1.057 | 0.051 |
| #3 | 220 | 394 | 219.3 | 0.098 | 0.790 | 218.2 | 1.101 | 226.1 | 1.066 | 0.058 |
| #4 | 258 | 449 | 250.0 | 0.098 | 0.813 | 243.4 | 1.119 | 251.0 | 1.092 | 0.081 |
| #5 | 265 | 475 | 264.4 | 0.084 | 0.789 | 262.1 | 1.108 | 267.1 | 1.099 | 0.088 |
| #6 | 315 | 544 | 302.8 | 0.100 | 0.819 | 314.1 | 1.072 | 308.2 | 1.097 | 0.086 |
| #7 | 340 | 597 | 332.3 | 0.114 | 0.805 | 326.9 | 1.125 | 335.0 | 1.100 | 0.088 |
| #8 | 350 | 641 | 356.8 | 0.094 | 0.772 | 346.4 | 1.133 | 355.5 | 1.114 | 0.101 |

^aCalculated from the PBG, assuming a solid volume fraction of 0.1 and *n*Ta₂O₅ = 2.0. ^bCalculated from plots of *λ*_{max}² vs sin²θ. ^cCalculated from plots of *λ*_{max} v *n*_{solvent}.

(1.633²*D*²*n*_{avg}²) of the linear plots allowed the estimation of *D*, *n*_{avg} and φ_{PMMA}, with the results for all eight PMMA colloidal crystals being in good general accord with expectations for a PMMA colloidal crystal with a solid volume fraction of around 74% in air (Table 2).

The normalized PBG bandwidths (Δ*λ*/*λ*_{max}, where Δ*λ* is the full width at half maximum of the reflectance peak) were near-identical for all eight batches of PMMA colloidal crystals ~0.073–0.077 and independent of colloid diameter (*D*), as expected due to the identical construction of the PMMA CC templates (Table 2). The angular frequencies of the [111] PBGs (ω = *a*/*λ*_{max}, where the lattice constant *a* = √2*D* for a fcc lattice) were calculated to be ~0.64 for all samples (Table 2), in perfect accord with a prediction from the simulated PBG structure diagram for the PMMA colloidal crystals (ω = 0.639, Figure S7). The PBG structure diagram shows a pseudo photonic band gap between the second and third bands along the L → Γ direction in reciprocal space, corresponding to the [111] direction in real space. The PBG blue-shifts to higher angular frequencies as the incident angle of light with respect to the [111] direction increases, consistent with the blue shift of PBG in the transmittance spectra of Figure 4c–e with increasing θ values.

Next, the optical properties of the Ta₂O₅ IOs prepared from the PMMA colloidal crystal templates were investigated. The rich structural color palette offered by the Ta₂O₅ inverse opals is evident from the digital photographs in Figure 4 for films of #2 Ta₂O₅ IO, #4 Ta₂O₅ IO, #5 Ta₂O₅ IO, #6 Ta₂O₅ IO, and #7 Ta₂O₅ IO in air and filled with ethanol.

When illuminated and viewed along the film normal (i.e., [111] direction), the films appeared colorless, violet, blue, green, and orange, respectively. The observation of such different colors confirmed the success of the colloidal crystal templating procedure, with #2 Ta₂O₅ IO having a PBG along the [111] direction at UV wavelengths (thus explaining its absence of visible color in air). After filling the macropores in the inverse opals with ethanol (*n*_{ethanol} = 1.361), the color of all samples red-shifted due to the corresponding increase in the average refractive index (*n*_{avg}) of the Ta₂O₅ IOs, with #2 Ta₂O₅ IO now showing a blue-green color at visible wavelengths. Some of the Ta₂O₅ IOs with larger macropore sizes (e.g., #6 Ta₂O₅ IO) became colorless after being filled with ethanol, indicating that the PBG along the [111] direction had red-shifted outside of the visible region. This red shift in the PBG position on filling the inverse opals with a solvent forms the basis for Ta₂O₅ IO thin-film-based liquid refractive sensors, as discussed below.

Figure Sa,b shows UV–vis reflectance and transmittance spectra, respectively, for #1 to #8 Ta₂O₅ IOs. All spectra were collected along the [111] direction. The data show that as the macropore diameter (*D*) in the Ta₂O₅ IOs increased, the PBG

position along the [111] progressively red-shifted, as predicted by eqs 5 and 6. The [111] PBG values for the Ta₂O₅ IOs were all around 68–69% of the [111] PBG values for the PMMA colloidal crystal templates, demonstrating that size control in the PMMA colloids allows the fabrication of tantalum (V) oxide inverse opal replicas with well-defined structural and optical properties. As with the PMMA colloidal crystals, the PBGs in the Ta₂O₅ IOs blue-shifted as the incident angle of light with respect to the [111] direction increased, as shown in Figure 5c–e. Plots of *λ*_{max}² vs sin²θ were linear (Figure 5f), with values of *D*, *n*_{avg} and φ_{Ta₂O₅} determined from the slopes and intercepts of the plots summarized in Table 3. Note that the calculated solid volume fractions (φ_{Ta₂O₅}) in the inverse opals were all much lower than 0.26 (the maximum void space in the PMMA colloidal crystal templates), which is explained by shrinkage and densification of the Ta₂O₅ network in the walls of the inverse opals after PMMA template removal by calcination. Interestingly, the Ta₂O₅ solid volume fraction increased with increasing diameter of PMMA colloids in the templates. This suggests that the interstitial voids in the PMMA colloidal crystals were harder to fill with the ethanolic TaCl₅ solution when the PMMA colloid diameters were small.

The normalized PBG bandwidths (Δ*λ*/*λ*_{max}) were near-identical for all eight batches of Ta₂O₅ inverse opals (all around 0.10, Table 3). The angular frequencies (ω = *a*/*λ*_{max}, where *a* = √2*D*) for the [111] PBGs for the Ta₂O₅ inverse opals were calculated to be ~0.76 (Table 3), similar to that predicted by PBG structure diagram calculations for a Ta₂O₅ IO with a solid volume fraction around 10% (Figure 6).

Figure 7a–c shows UV–vis transmittance spectra for the #4, #6, and #8 Ta₂O₅ IO films in air (*n* = 1.00), methanol (*n* = 1.329), ethanol (*n* = 1.361), *n*-heptane (*n* = 1.388), dichloromethane (*n* = 1.4241), carbon tetrachloride (*n* = 1.4601), and benzene (*n* = 1.501). Filling the macropores of the Ta₂O₅ inverse opals increased the refractive index (*n*_{avg}) of the inverse opals and red-shifted the PBG position along [111] direction (as seen visually in Figure 4), with the magnitude of the red shift being proportional to the refractive index of the solvent. Figure 7d confirmed a linear relationship between the [111] PBG position and the solvent refractive index for the three different Ta₂O₅ IO films, which can be explained by the substitution of [φ_{solid}*n*_{solid} + (1 – φ_{solid})*n*_{void}] for *n*_{avg} in eq 6.

$$\lambda_{\max} = 1.633D\phi_{\text{solid}}n_{\text{solid}} + 1.633D(1 - \phi_{\text{solid}})n_{\text{void}} \quad (7)$$

where *n*_{void} is the refractive index of the liquid filling the macropores in the Ta₂O₅ inverse opals. Equation 7 predicts a plot of *λ*_{max} vs *n*_{void} (i.e., *n*_{solvent}) should be linear with a slope = 1.633*D*(1 – φ_{solid}) and *y*-axis intercept = 1.633*D*φ_{solid}*n*_{solid}. By

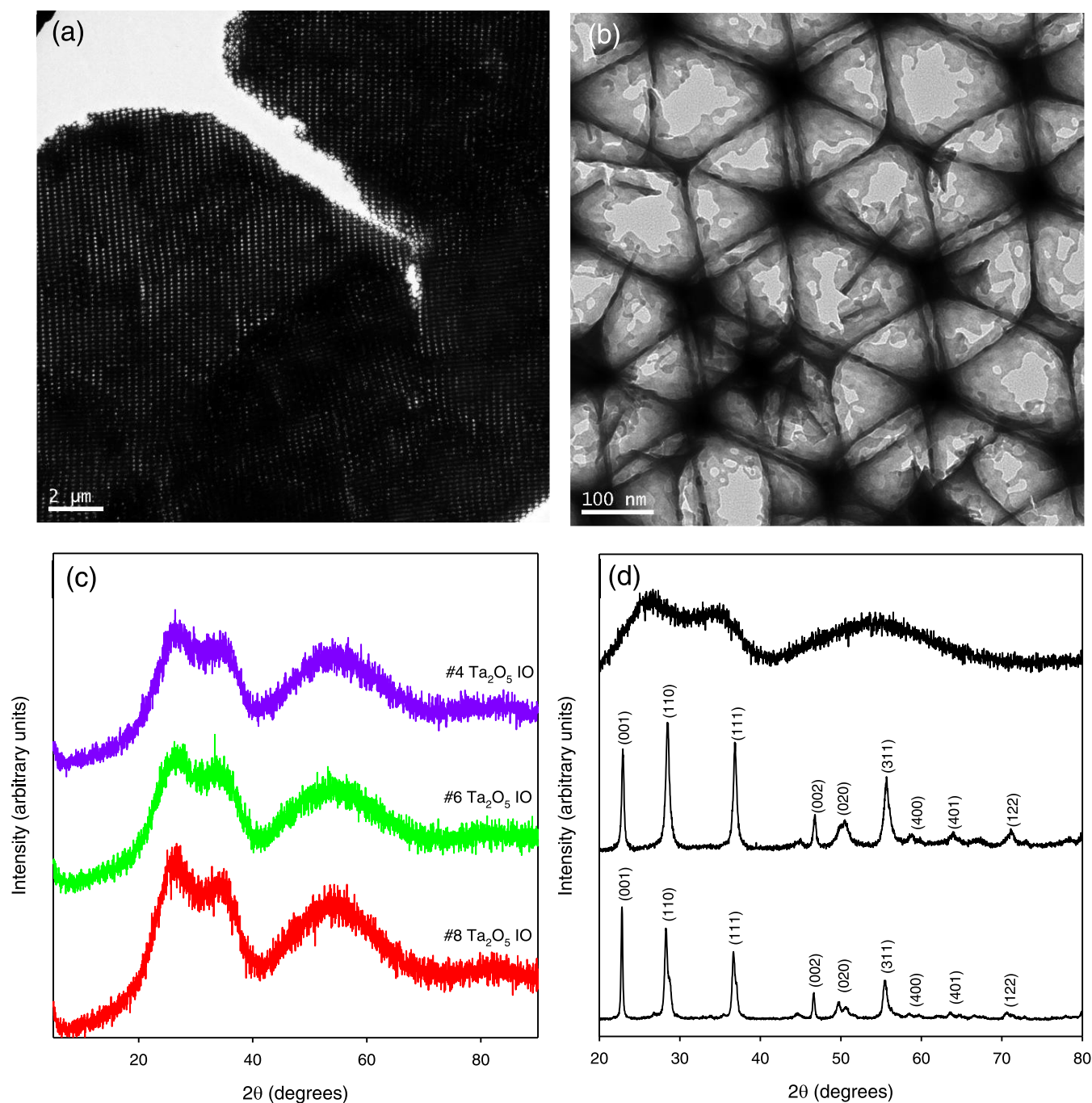


Figure 3. (a, b) TEM images for #6 Ta₂O₅ IO. (c) XRD patterns for selected Ta₂O₅ IO powders prepared by calcination at 550 °C for 4 h. (d) XRD patterns for #6 Ta₂O₅ IO calcined at selected temperatures (550, 700, and 800 °C, from top to bottom, respectively).

simple mathematical rearrangement, the following equations can be obtained:

$$D = \frac{\text{slope} \times n_{\text{solid}} + \text{intercept}}{1.633 \times n_{\text{solid}}} \quad (8)$$

$$\phi_{\text{solid}} = \frac{\text{intercept}}{\text{slope} \times n_{\text{solid}} + \text{intercept}} \quad (9)$$

Using the experimentally determined slopes and intercepts of the linear regressions in (Figure 7d), values of D and $\phi_{\text{Ta}_2\text{O}_5}$ for the different Ta₂O₅ IOs were calculated using eqs 8 and 9, with the results summarized in Table 3. The calculated macropore

diameters (D) were in excellent accord with values measured by SEM on the (111) planes, while the $\phi_{\text{Ta}_2\text{O}_5}$ values were all around 0.1 (indicating that the inverse opals were approximately 10% Ta₂O₅ and 90% void by volume). It should be pointed out the red shift in the PBG position with solvent refractive index was sufficient to readily distinguish methanol ($n = 1.329$) and water ($n = 1.333$) or ethanol ($n = 1.361$) and acetone ($n = 1.359$).

Fabrication and Characterization of Ta₃N₅ Inverse Opals. Since tantalum (V) nitride photocatalysts show great promise in visible-light-driven photocatalysis due to their narrow electronic band gap ($E_g = 2.0\text{--}2.1$ eV), it was of interest to see if Ta₃N₅ IOs could be prepared from Ta₂O₅ IO thin films and powders by thermal nitridation in NH₃ at 700 °C. For this

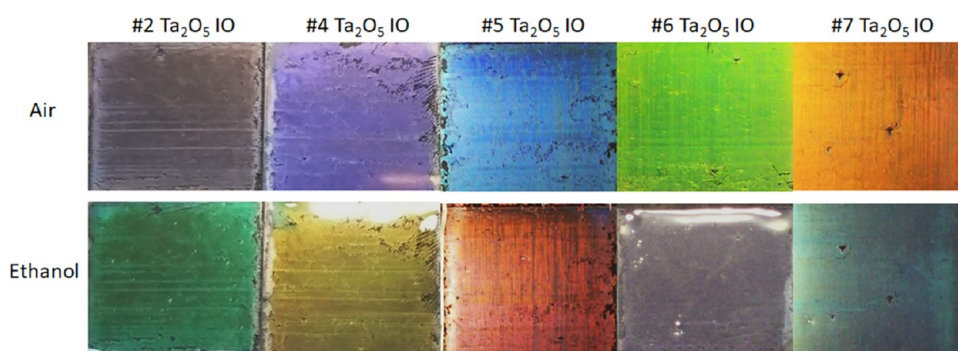


Figure 4. Digital photographs of selected Ta_2O_5 inverse opal thin films in air ($n = 1.000$) and ethanol ($n = 1.361$). Note the large red shift in the color of the films on filling the macropores in the inverse opals with ethanol.

purpose, we used #7 Ta_2O_5 IO films (on quartz microscope slides) and powders. The #7 Ta_2O_5 IO powder was white (BET surface area $39.1 \text{ m}^2 \text{ g}^{-1}$), with some angle-dependent structural color observed in flatter pieces of sufficient size to diffract light uniformly toward the observer. Following thermal nitridation in NH_3 , both the thin film and the powder samples possessed an orange base color, confirming the successful nitridation of Ta_2O_5 IOs to Ta_3N_5 IOs (Ta_3N_5 absorbs light strongly below 600 nm and reflects orange and red light). The BET specific surface area of the #7 Ta_3N_5 IO powder was $36.7 \text{ m}^2 \text{ g}^{-1}$, lower than that of the #7 Ta_2O_5 IO precursor but much higher than that of a noninverse opal Ta_3N_5 reference photocatalyst ($8.4 \text{ m}^2 \text{ g}^{-1}$) prepared by thermal nitridation of a commercial Ta_2O_5 powder ($2.8 \text{ m}^2 \text{ g}^{-1}$) supplied by Wako Chemicals.

Figure 8a–c shows SEM images for the #7 Ta_3N_5 IO film. The images show that the 3DOM structure of the parent #7 Ta_2O_5 IO film was retained after the thermal nitridation treatment, with the sample showing good order along the [111] direction. The macropore size (D) in #7 Ta_3N_5 IO was estimated to be ~ 340 nm, much smaller than the D value of ~ 380 nm for #7 Ta_2O_5 IO. Clearly, substantial shrinkage of the inverse opal lattice occurred on transforming Ta_2O_5 in the walls of the inverse opal to Ta_3N_5 . The XRD patterns for the #7 Ta_3N_5 IO powder and Ta_3N_5 reference powder were similar (Figure 8d), showing peaks due to orthorhombic Ta_3N_5 (space group $Cmcm$, $a = 3.8862 \text{ \AA}$, $b = 10.2118 \text{ \AA}$, and $c = 10.2624 \text{ \AA}$, JCPDS Card No. 79-1533).^{58,59} No peaks due to Ta_2O_5 or oxynitride phases such as TaON were present in the XRD patterns, implying complete conversion of the Ta_2O_5 precursors to phase-pure Ta_3N_5 . The nitrogen and oxygen contents in the #7 Ta_3N_5 IO powder determined by O/N analysis were 10.47 and 1.00 wt %, with the balance being Ta (88.53 wt %). These nitrogen and tantalum contents were very close to the theoretical values for Ta_3N_5 (N 11.43 wt %, Ta 88.57 wt %). The small amount of oxygen in the sample was possibly due to some oxidation with air exposure or residual amorphous Ta_2O_5 . The Ta_3N_5 reference powder possessed a similar composition as Ta_3N_5 IO #5, with the contents of N, O, and Ta being 10.17, 1.38, and 88.45 wt %, respectively.

Figure 8e shows the UV–vis reflectance spectrum for #7 Ta_3N_5 IO film in air ($n = 1.00$), ethanol ($n = 1.361$), DCM ($n = 1.424$), and benzene ($n = 1.501$). Figure 8f shows the color of the film in air and ethanol. The [111] PBG in air was at 562 nm, approximately 40 nm lower than the value for the corresponding Ta_2O_5 IO in air (601 nm). As noted above, the macropore diameter (D) value decreased by $\sim 14\%$ on converting #7 Ta_2O_5 IO to #7 Ta_3N_5 IO, which explains the lower PBG position for the latter. Even though Ta_3N_5 has a refractive index (n) of 2.9,

much higher than that of Ta_2O_5 ($n = 2.1$), the decrease in D with converting the Ta_2O_5 IO to Ta_3N_5 IO meant that the [111] PBG for the #7 Ta_3N_5 IO was lower than that of the #7 Ta_2O_5 IO precursor. However, the normalized bandwidth $\Delta\lambda/\lambda_{\text{max}}$ of the [111] PBG peak for #7 Ta_3N_5 IO was 0.13, almost twice that of #7 Ta_2O_5 IO ($\Delta\lambda/\lambda_{\text{max}} = 0.076$), which directly reflects the higher refractive index of Ta_3N_5 compared to Ta_2O_5 . As with the Ta_2O_5 IO films, the PBG along the [111] direction in the #7 Ta_3N_5 IO film red-shifted on filling the macropores with organic solvents. By plotting the PBG position vs the refractive index of the medium in the macropores, a good linear relationship was obtained. Using the slope and intercepts, together with eqs 8 and 9, the D , $\phi_{\text{Ta}_3\text{N}_5}$ and n_{avg} values for #7 Ta_3N_5 IO in air were calculated to be 252, 0.045, and 1.103, respectively. The calculated D value of 252 nm was quite a bit smaller than the value of ~ 340 nm estimated by SEM (when viewing the samples along the [111] direction). The UV–vis data measures the periodicity along the [111] direction, from which D is then calculated. The lower value of D determined by UV–vis suggests that on converting amorphous Ta_2O_5 IO to nanocrystalline Ta_3N_5 IO, the macropores in the inverse opals collapsed slightly (by $\sim 20\%$), thus reducing the interplanar spacing along the [111] direction, while leaving the apparent diameter of the macropores in the (111) planes unchanged. Partial collapse along the [111] direction is not surprising, given the fragile connections between Ta_3N_5 crystallites in the walls of the inverse opals and the low solid volume fraction in the sample ($\sim 10\%$ solid). The cross-sectional image of the #7 Ta_3N_5 IO film (Figure 8c) supports this hypothesis, with the macropores appearing slightly elliptical rather than spherical when the film was viewed in cross section.

Photocatalytic Hydrogen Production Tests Using Ta_3N_5 Inverse Opals. Ta_3N_5 has an electronic band gap ($E_g = 2.0\text{--}2.1 \text{ eV}$), with the valence band (VB) and conduction band (CB) levels around $+1.58 \text{ V}$ and -0.52 V , respectively, vs NHE. These band edge positions are sufficient to allow water oxidation ($\text{O}_2/\text{H}_2\text{O}$, $E = +0.82 \text{ V}$ at pH 7) and proton reduction (H^+/H_2 , $E = -0.41 \text{ V}$ at pH 7), respectively, under band gap excitation.⁶⁰ These properties make Ta_3N_5 photocatalysts very promising materials for solar-driven water splitting. While overall water splitting over Ta_3N_5 photocatalysts is thermodynamically favorable, rates of H_2 production are generally very low due to rapid electron–hole pair recombination following photoexcitation. Therefore, to achieve meaningful hydrogen production rates, researchers use alcohols (such as methanol) as sacrificial hole scavengers and decorate the surface of Ta_3N_5

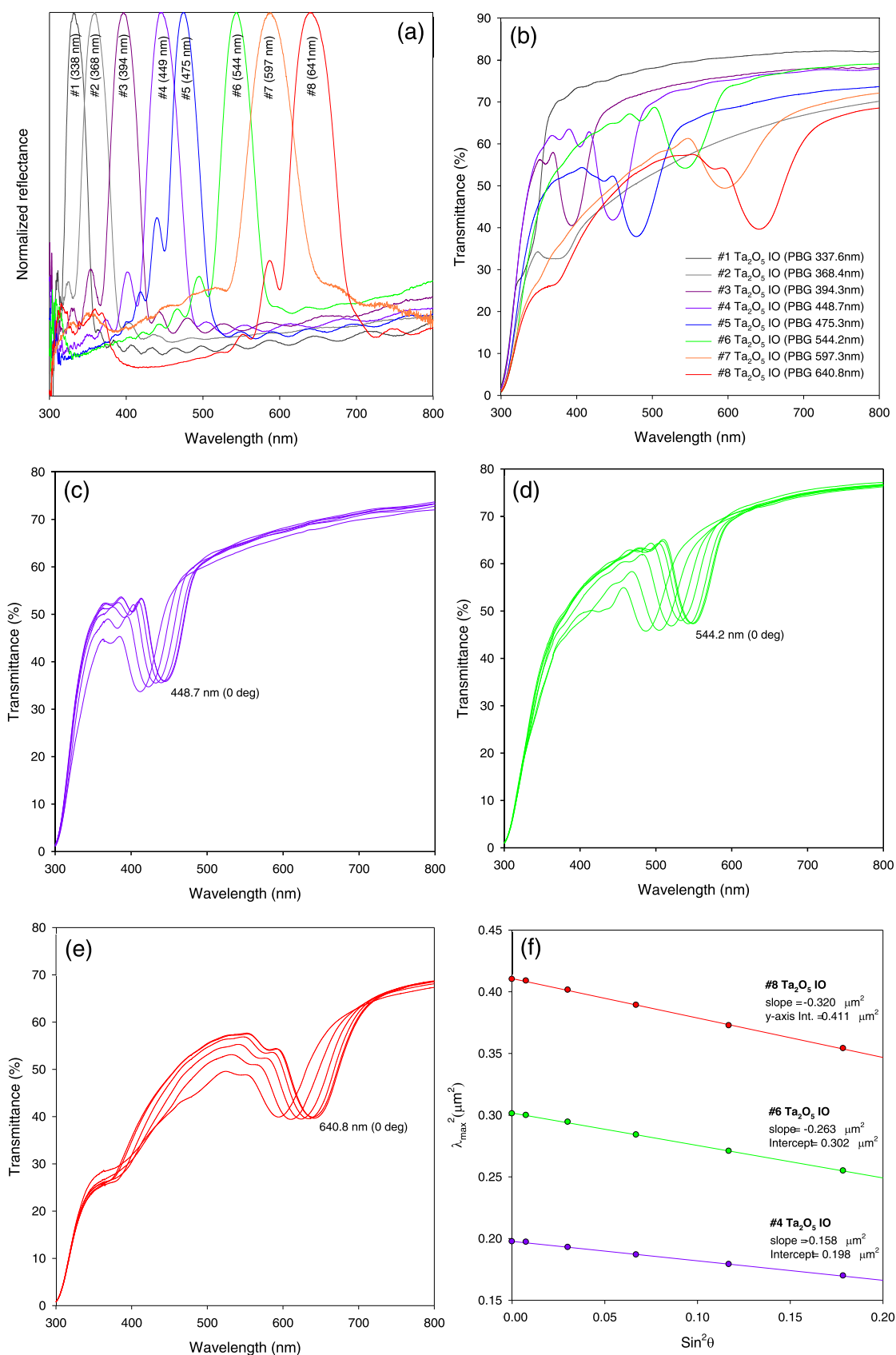


Figure 5. Optical characterization of Ta₂O₅ inverse opals. (a) Normalized UV–vis reflectance spectra for the different Ta₂O₅ IOs in air. (b) UV–vis transmittance spectra for the different Ta₂O₅ IOs in air. All data in panels (a, b) were collected along the [111] direction. UV–vis transmittance spectra collected at different angles ($\theta = 0–25^\circ$ in 5° increments) with respect to the [111] direction for (c) #4 Ta₂O₅ IO, (d) #6 Ta₂O₅ IO, and (e) #8 Ta₂O₅ IO. (f) Plot of the λ_{\max}^2 vs $\sin^2 \theta$ for the samples in panels (c–e).

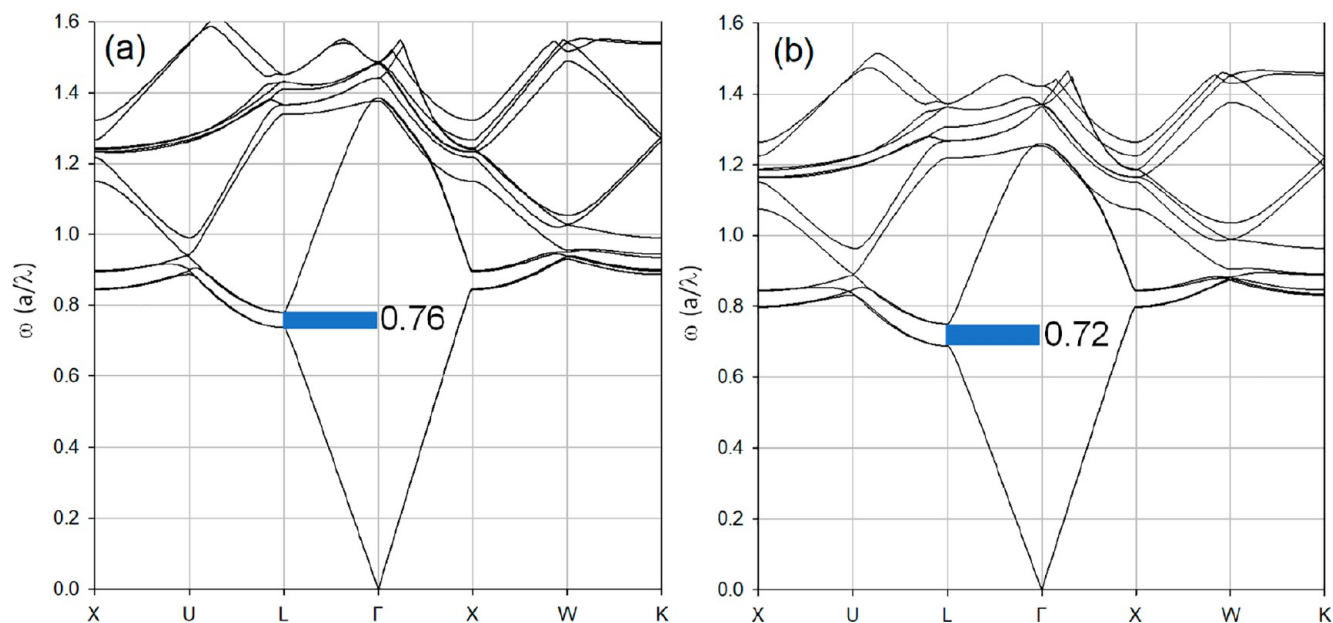


Figure 6. Photonic band gap structure diagrams for Ta_2O_5 inverse opals in air. A pseudo PBG occurs along $L \rightarrow \Gamma$ (i.e., the $[111]$ direction in real space) at (a) $\omega = 0.76$ and (b) $\omega = 0.72$ for Ta_2O_5 IOs with solid volume fractions of 10 and 15%, respectively.

photocatalysts with platinum nanoparticles (thus creating cathodic sites for H_2 evolution).

In this work, an in situ photodeposition method was used to prepare 1 wt % Pt/ Ta_3N_5 photocatalysts. Briefly, #7 Ta_3N_5 IO or a reference Ta_3N_5 powder photocatalyst, denoted herein as Ta_3N_5 (bulk) and prepared by nitridation of a commercial Ta_2O_5 powder, were loaded into a glass photoreactor containing a small amount of $\text{H}_2\text{PtCl}_6 \cdot 3\text{H}_2\text{O}$ dissolved in 10 vol % methanol (2 mL of methanol, 18 mL of water). After degassing the system, the magnetically stirred Ta_3N_5 photocatalyst dispersion was then irradiated using a Xe lamp with a UV cutoff filter ($\lambda \geq 420$ nm). In the initial stages of photoexcitation, valence band holes were consumed by methanol or water oxidation, while conduction band electrons reduced adsorbed cationic Pt species to Pt^0 , leading to the surface decoration of the Ta_3N_5 photocatalysts with small 1–3 nm sized platinum nanoparticles. The platinum nanoparticles subsequently acted as sites for photocatalytic hydrogen evolution, with H_2 production being monitored as a function of Xe lamp irradiation time to determine H_2 evolution rates for the 1 wt % Pt/#7 Ta_3N_5 IO and 1 wt % Pt/ Ta_3N_5 (bulk) powder photocatalysts.

Figure 9a–d shows TEM images for 1 wt % Pt/#7 Ta_3N_5 IO photocatalyst prepared by the in situ photodeposition method (i.e., formed during the photocatalytic methanol reforming tests). TEM images for the 1 wt % Pt/ Ta_3N_5 (bulk) powder photocatalyst are shown in Figure 9e,f. In each case, small and well-dispersed Pt nanoparticles could be seen on the Ta_3N_5 supports, reflecting the well-known strong metal–support interaction between Pt and Ta_3N_5 .^{61,62} In the higher magnification TEM images of the Pt/#7 Ta_3N_5 IO sample, lattice fringes with an interplanar spacing of 0.428 nm could be observed, corresponding to the (110) plane of Ta_3N_5 .⁵⁸ In the TEM images of both samples, pores could be seen in the Ta_3N_5 supports, which were absent in the Ta_2O_5 precursors. The appearance of these pores following Ta_2O_5 nitridation to Ta_3N_5 reflects the fact that although Ta_2O_5 and Ta_3N_5 both formally contain Ta(V), Ta_3N_5 contains fewer anions per Ta atom (1.67 N^{3-} anions/Ta atom) than Ta_2O_5 (2.5 O^{2-} anions/Ta atom).

Accordingly, nitridation will cause a decrease in the solid volume, which manifests as mesopores (2–50 nm) in the Ta_3N_5 products, as seen in the TEM images of Figure 9.

The XRD patterns for the #7 Ta_3N_5 IO and 1 wt % Pt/#7 Ta_3N_5 IO samples were identical (Figure 10a), being typical for orthorhombic Ta_3N_5 (JCPDS Card No. 79-1533).^{58,59} This confirmed that the Ta_3N_5 IO support was stable under the conditions used for the photocatalytic H_2 production tests in aqueous methanol. No diffraction peaks were seen for platinum in the XRD pattern of the 1 wt % Pt/ Ta_3N_5 IO photocatalyst, reflecting the low platinum loading and also the severe line-broadening in 1–3 nm sized nanoparticles.⁶³

X-ray photoelectron spectroscopy (XPS) was next applied to examine the near-surface region chemical composition of the #7 Ta_2O_5 IO, #7 Ta_3N_5 IO, and 1 wt % Pt/#7 Ta_3N_5 IO samples. The technique probes the top few nanometers in materials.⁵⁶ The XPS survey spectrum for the Ta_2O_5 IO (Figure 10b) showed peaks due to Ta, O, and C, the latter mainly being due to adventitious hydrocarbons and surface carbonates. Nitridation gave new peaks due to N, while the in situ photodeposition step to form the Pt/ Ta_3N_5 IO photocatalyst gave some additional weak peaks due to Pt. Figure 10c shows Ta 4f spectra for the different samples. The Ta_2O_5 IO showed peaks at 26.3 and 28.2 eV in a characteristic 4:3 area ratio, which could readily be assigned to the $4f_{7/2}$ and $4f_{5/2}$ signals, respectively, of Ta^{5+} in Ta_2O_5 .^{28,64} The corresponding O 1s spectrum for the Ta_2O_5 IO (Figure 10d) showed the presence of two components, an intense peak at 530.6 eV due to lattice oxygen (O^{2-}) in Ta_2O_5 , and a smaller peak at 532.3 eV which is assigned to surface hydroxyl or carbonate species.^{56,64,65} The Ta 4f spectra for the Ta_3N_5 IOs and Pt/ Ta_3N_5 IOs samples showed two sets of peaks. An intense set of peaks at 25.5 and 27.4 eV in a 4:3 area ratio could readily be assigned to the Ta $4f_{7/2}$ and $4f_{5/2}$ signals, respectively, of Ta^{5+} cations in Ta_3N_5 .^{60,66,67} Since nitrogen is less electronegative than oxygen, the Ta 4f signals for Ta^{5+} in Ta_3N_5 appear at lower binding energies than the Ta 4f signals for Ta^{5+} in Ta_2O_5 . The weaker set of peaks at 26.4 and 28.3 eV are assigned to a thin surface Ta(V) oxide phase formed through air

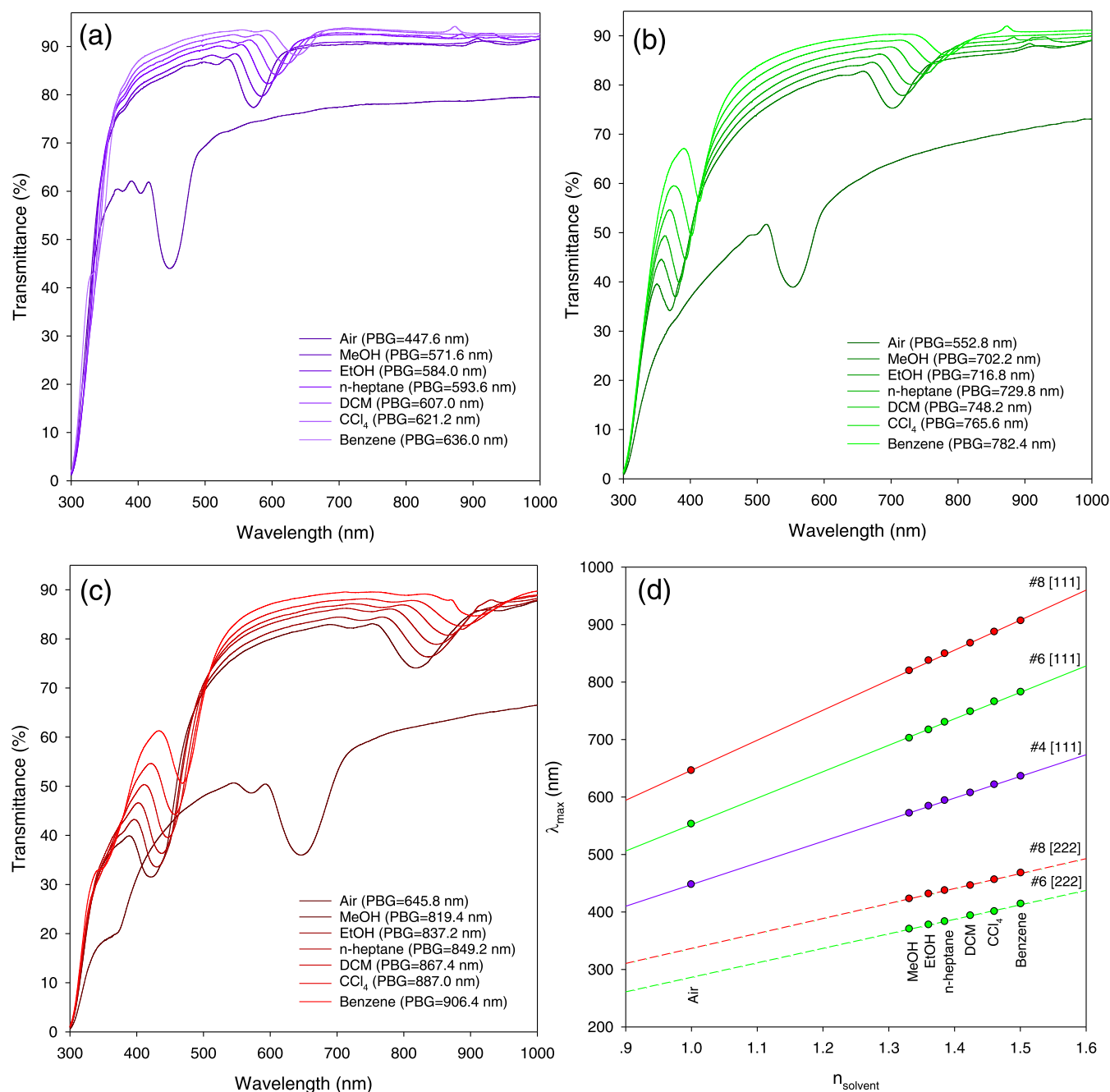


Figure 7. UV-vis transmittance spectra collected along the [111] direction for selected Ta₂O₅ inverse opal thin films in air and different organic solvents. (a) #4 Ta₂O₅ IO, (b) #6 Ta₂O₅ IO, and (c) #8 Ta₂O₅ IO. (d) Plot of the photonic band gap position (λ) vs refractive index of the medium in the macropores for selected Ta₂O₅ inverse opals.

contact.^{68–70} Evidence for such a thin surface oxide phase was verified by the presence of oxygen in the XPS survey spectra of the Ta₃N₅ IO samples and also multiple oxygen species in the core-level O 1s spectra of the samples. The N 1s spectra for #7 Ta₃N₅ IO and 1 wt % Pt/#6 Ta₃N₅ IO (Figure 10e) showed a single peak at 397.0 eV, typical for lattice nitrogen (formally N³⁻) in Ta₃N₅.⁶⁰ The core-level Pt 4f spectrum for 1 wt % Pt/#7 Ta₃N₅ IO was dominated by peaks at 71.2 and 74.5 eV in a 4:3 area ratio, typical for Pt⁰ (Figure 10f).⁷¹ It is worth noting that the Pt 4f spectrum overlaps the Ta 5s region, but since the Ta 5s signal is very broad, it does not interfere with the determination of the Pt valence state in the 1 wt % Pt/#7 Ta₃N₅ IO photocatalyst. The data confirms the successful photodeposition

of metallic Pt nanoparticles on the #7 Ta₃N₅ IO support during the photocatalytic hydrogen production tests. Further, the speciation of Ta and N in the Ta₃N₅ IO support was unchanged by Pt nanoparticle photodeposition during the H₂ production experiments, indicating that the Ta₃N₅ IO was photocatalytically stable (i.e., no loss of N occurred during the hydrogen production tests, which might have led to low-valent Ta states and a change in optical absorption characteristics). This was further verified by an O/N analysis performed on the 1 wt % Pt/#7 Ta₃N₅ IO catalyst, with the N and Ta contents being very similar to the data reported above for #7 Ta₃N₅ IO prior to the H₂ production tests. XPS data collected for the ref 1 wt % Pt/Ta₃N₅(bulk) powder photocatalyst (not shown) were very

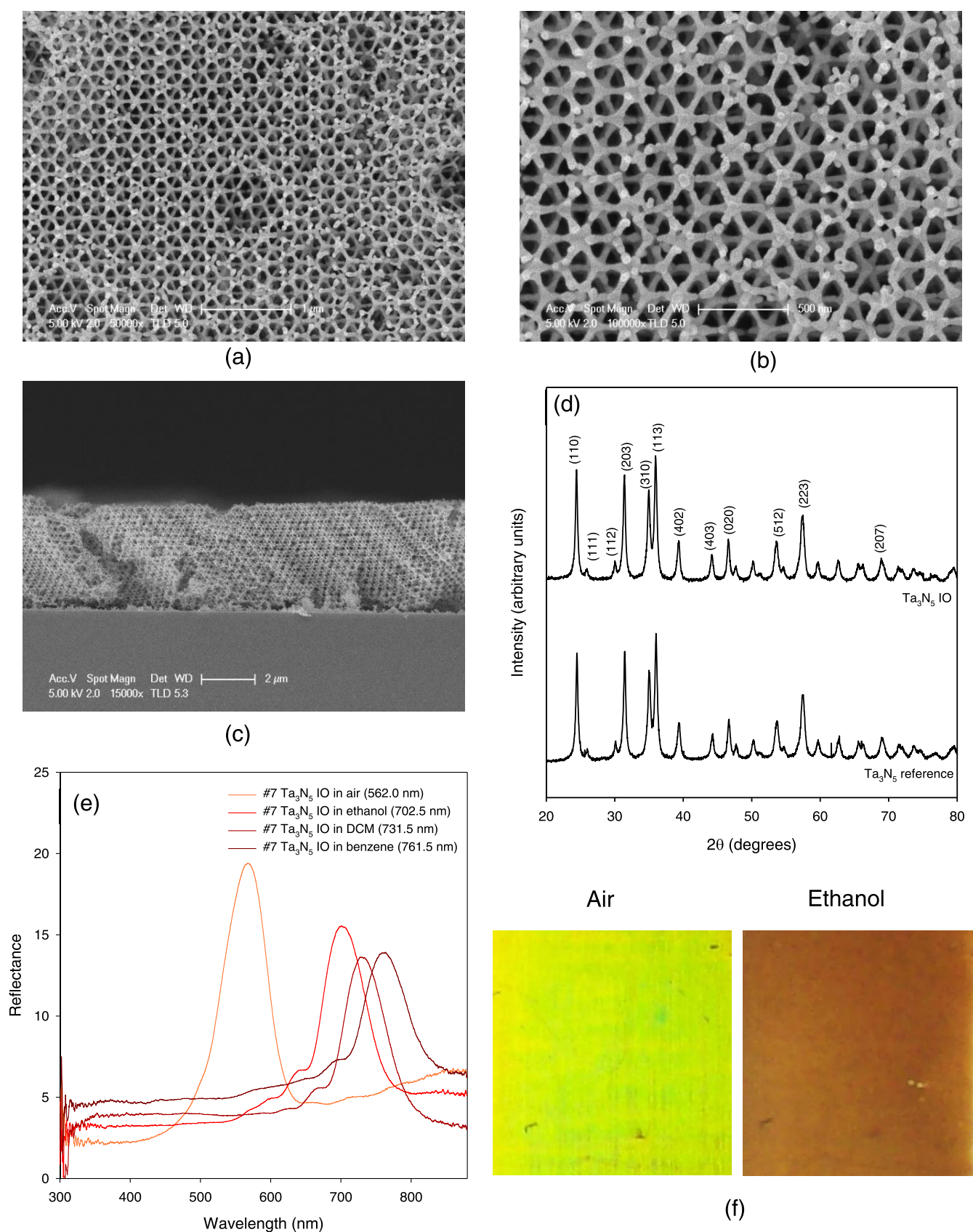


Figure 8. (a–c) SEM images for the #7 Ta₃N₅ IO thin film. (d) XRD patterns for selected Ta₃N₅ IO powders. (e) Reflectance spectra for a #7 Ta₃N₅ IO film in air and selected organic solvents. (f) Digital photographs for the #7 Ta₃N₅ IO film in air and ethanol.

similar to that for the 1 wt % Pt/#7 Ta₃N₅ IO photocatalyst. ICP analysis confirmed that the Pt loading in the 1 wt % Pt/#7 Ta₃N₅

IO and 1 wt % Pt/Ta₃N₅(bulk) photocatalysts were similar (~1 wt %).

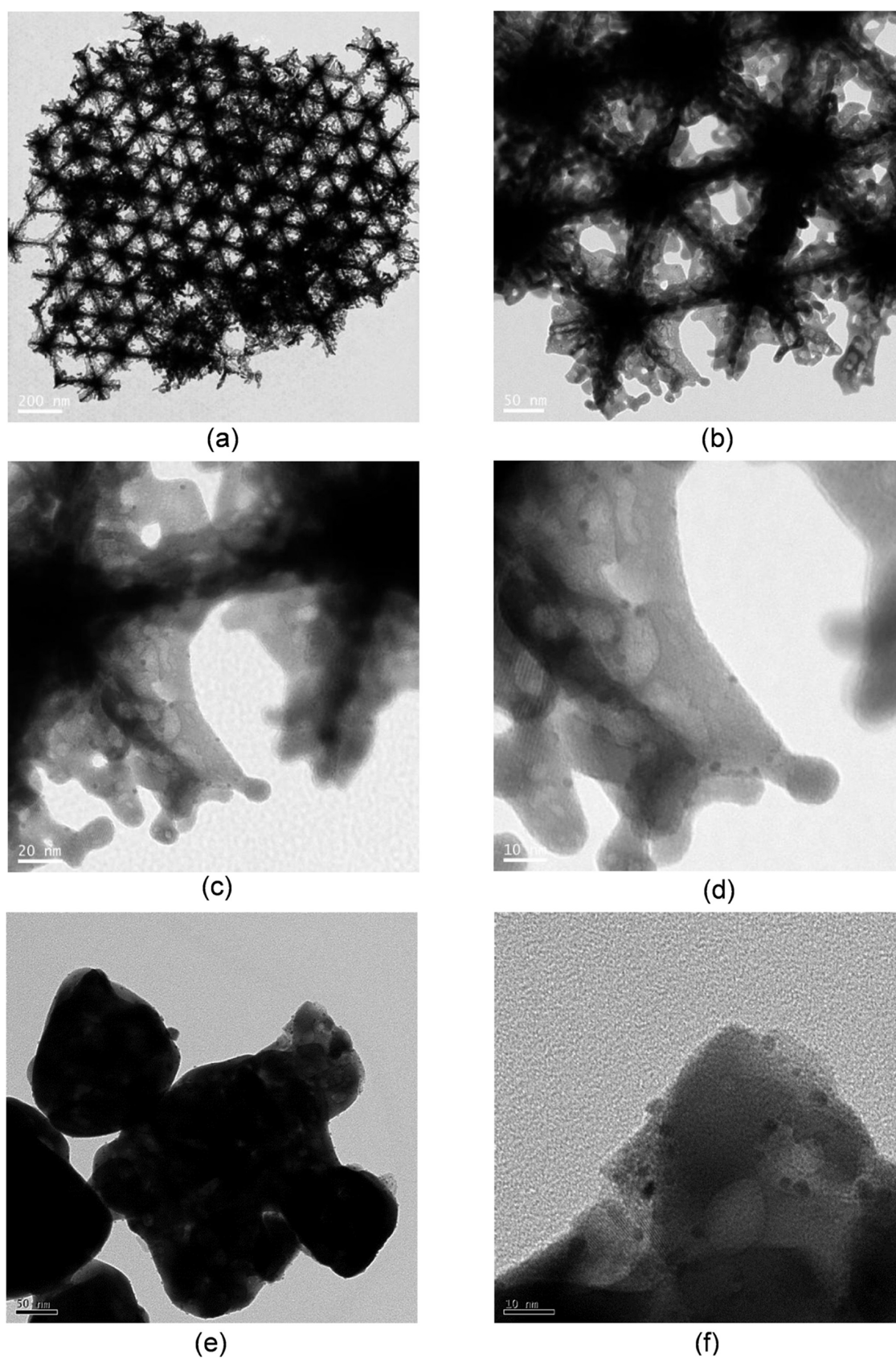


Figure 9. TEM images of (a–d) 1 wt % Pt/#7 Ta₃N₅ IO photocatalyst prepared using the in situ photodeposition method and (e, f) 1 wt % Pt/Ta₃N₅(bulk) photocatalyst prepared using the in situ photodeposition method.

The photocatalytic hydrogen production activities of #7 Ta₂O₅ IO, #7 Ta₃N₅ IO, and Ta₃N₅(bulk) powder photo-

catalysts were evaluated in aqueous 10 vol % methanol solutions under visible-light irradiation supplied by a 300 W Xe lamp with

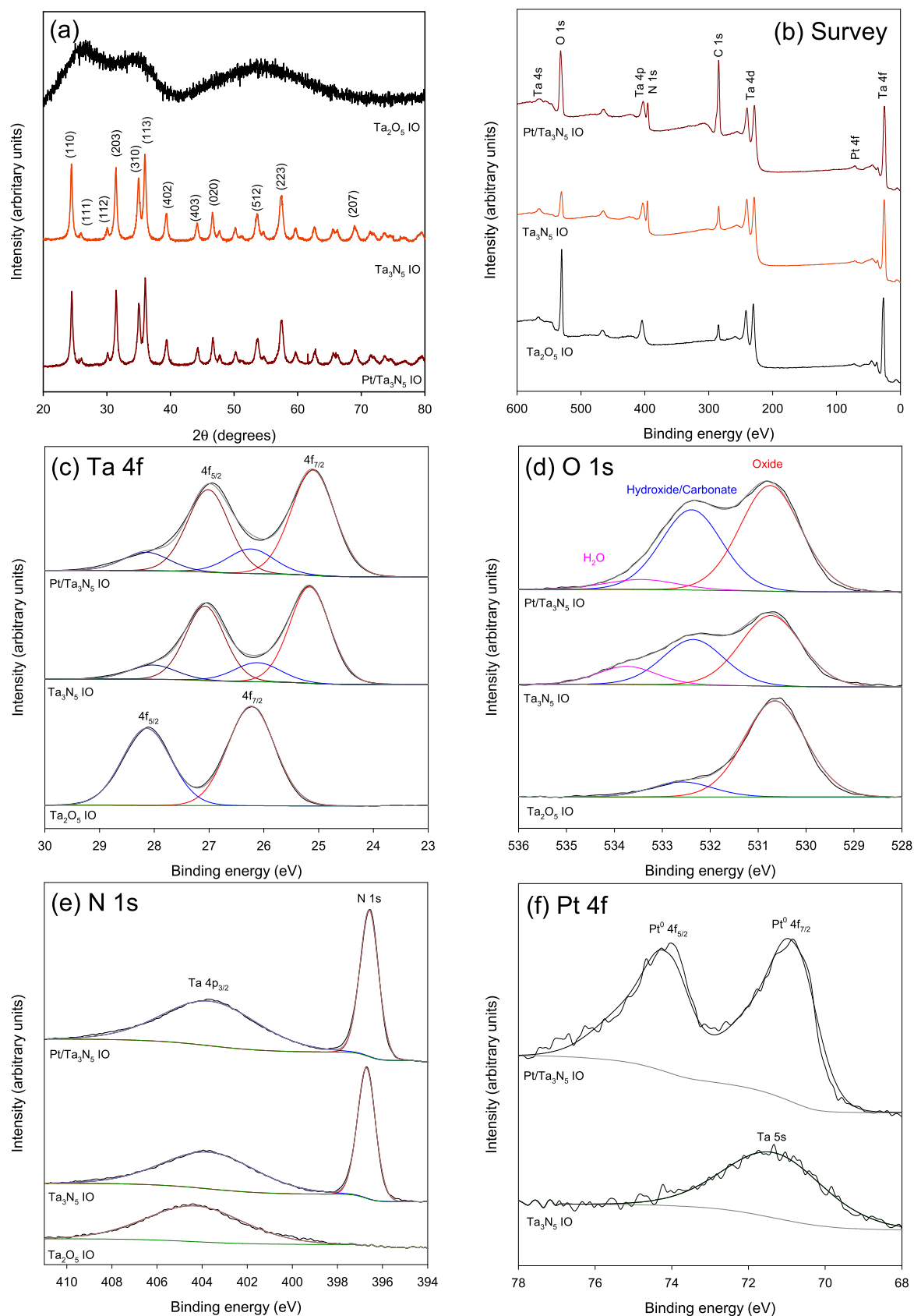


Figure 10. (a) XRD patterns for the #7 Ta₃N₅ IO and 1 wt % Pt/#7 Ta₃N₅ IO photocatalysts. XPS spectra for selected photocatalysts: (b) survey spectra, (c) Ta 4f spectra, (d) O 1s spectra, (e) N 1s spectra, and (f) Pt 4f spectra.

a 420 nm cutoff filter ($\lambda \geq 420$ nm). Results of the photocatalytic tests are shown in Figure 11. The #7 Ta₂O₅ IO photocatalyst

showed negligible H₂ production activity under the applied testing conditions, even in the presence of H₂PtCl₆·3H₂O. This

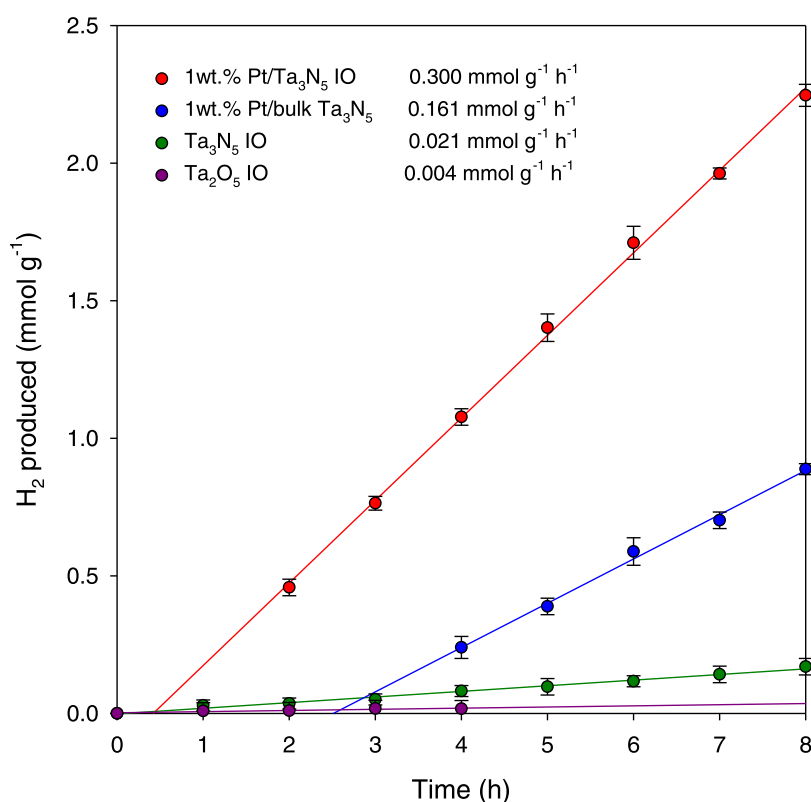


Figure 11. Hydrogen production data for selected photocatalysts in a 10:90 v/v methanol–water mixture under visible-light irradiation (300 W Xe lamp with ≥ 420 nm cutoff filter).

was expected, since Ta₂O₅ has a wide band gap of 3.9–4.0 eV and thus should not be photoexcited under visible light. The bare #7 Ta₃N₅ IO photocatalyst (in the absence of H₂PtCl₆·3H₂O) showed a low H₂ production rate of 21 $\mu\text{mol g}^{-1} \text{h}^{-1}$ with no induction period, confirming that Ta₃N₅ is able to generate H₂ under the testing conditions used in this work. The rate of H₂ production increased dramatically to 300 $\mu\text{mol g}^{-1} \text{h}^{-1}$ for the #7 Ta₃N₅ IO photocatalyst when H₂PtCl₆·3H₂O was present (due to the in situ formation of the 1 wt % Pt/#7 Ta₃N₅ IO photocatalyst), with an induction period of ~ 25 min duration with no H₂ production observed at the start of the testing.

The induction period is associated with the reduction of adsorbed cationic platinum species (formed by adsorption of aqueous PtCl₆²⁻) to Pt⁰ nanoparticles on the photocatalyst surface, which then acted as cathodic sites for H₂ production. During the photocatalytic reaction, electrons photoexcited into the conduction band of Ta₃N₅ will migrate onto the Pt nanoparticles, thus transforming H⁺ to H₂ (i.e., 2H⁺ + 2e⁻ (CB) \rightarrow H₂), while valence band holes will be consumed by methanol oxidation (CH₃OH + 2h⁺ (VB) \rightarrow CH₃CHO + 2H⁺, as well as acetaldehyde oxidation) and also water oxidation (H₂O + 2h⁺ (VB) \rightarrow O₂ + 2H⁺).^{71–74} By this approach, electron–hole pair recombination in the Ta₃N₅-based photocatalysts can be minimized, thus boosting H₂ production rates. In the absence of Pt nanoparticles, electrons will accumulate in the conduction band of Ta₃N₅, explaining why the bare Ta₃N₅ IO had very modest H₂ evolution activity in comparison with the in situ-generated 1 wt % Pt/#7 Ta₃N₅ IO photocatalyst.^{72,75–78} After the short induction period, the 1 wt % Pt/#7 Ta₃N₅ IO photocatalyst generated H₂ in a linear manner under visible-light irradiation, implying excellent photocatalytic stability. The in situ-generated 1 wt % Pt/Ta₃N₅(bulk) photocatalyst was less

active than the 1 wt % Pt/#7 Ta₃N₅ IO photocatalyst, delivering a hydrogen production rate of 161 $\mu\text{mol g}^{-1} \text{h}^{-1}$ following a longer induction period of around 150 min. The Ta₃N₅(bulk) photocatalyst had a BET surface area of only 8.4 m² g⁻¹, much lower than that of the #7 Ta₃N₅ IO photocatalyst (36.7 m² g⁻¹). The lower surface area of the Ta₃N₅(bulk) photocatalyst explains the longer induction time before any H₂ production was observed, since the reduction of cationic Pt species to active Pt⁰ would naturally take longer on a photocatalyst of low surface area. The higher surface area of the 1 wt % Pt/Ta₃N₅(bulk) photocatalyst was also expected to allow excellent Pt nanoparticle dispersion while also offering more surface sites for methanol and water oxidation, thus boosting the photocatalytic activity. To understand the effect of surface area on performance, we normalized the photocatalytic H₂ production rates (in $\mu\text{mol g}^{-1} \text{h}^{-1}$) against the BET specific surface area of the photocatalysts (in m² g⁻¹). The resulting area normalized H₂ production rates for the 1 wt % Pt/#7 Ta₃N₅ IO photocatalyst and 1 wt % Pt/Ta₃N₅(bulk) photocatalyst were 8.18 and 19.26 $\mu\text{mol m}^{-2} \text{h}^{-1}$, respectively. Clearly, the advantage of the inverse opal architecture is to provide a high surface area form of Ta₃N₅ that allows enhanced H₂ production performance, even though the bulk powder was more active per unit area. The latter is explained by the low surface area powder having increased crystallinity, thus less bulk and surface defects for charge trapping. Pt particle size effects were not expected to be the reason for the different H₂ production activity (in mol g⁻¹ h⁻¹) between Pt/Ta₃N₅ IO and Pt/Ta₃N₅(bulk). Previous published work by our group has shown that cocatalyst particle size does not influence the rate of H₂ production over M/TiO₂ photocatalysts (M = Pd, Pt, Au).⁷⁹ Hence, it is not expected that small differences in Pt nanoparticle size effects were

responsible for the large difference in H₂ production rates (in mol g⁻¹ h⁻¹) seen for the Pt/Ta₃N₅ IO and Pt/Ta₃N₅(bulk) photocatalysts. Rather, the specific surface area of the Ta₃N₅ supports in each photocatalyst was the determining factor.

The H₂ production rate realized in this work of 300 μmol g⁻¹ h⁻¹ for the 1 wt % Pt/#7 Ta₃N₅ IO photocatalyst is among the highest yet reported for a Ta₃N₅-based visible-light-driven photocatalyst (Table S1).^{69,80–84} The photocatalytic tests in the current work utilized Ta₃N₅ IO powders. With a view toward further improving H₂ production rates, we are now attempting to exploit “slow photon” phenomena at the edges of the PBGs in Ta₃N₅ IO thin films. Previous studies of other inverse opal semiconductor systems have shown that by coupling the electronic absorption edge of the semiconductor with the red edge of the [111] PBG (i.e., the edge where the electric field of the incident light is localized on the semiconductor rather than the macropore), the group velocity of light in the semiconductor can be slowed enormously, leading to increased photon-semiconductor interactions (enhanced absorption due to the path length of light in the semiconductor being increased), leading to large enhancements in photocatalytic activity.^{85–88} The high-quality Ta₂O₅ IO films and Ta₃N₅ IO films produced in this study provide a perfect foundation for realizing “slow photon photocatalytic amplification” of H₂ production over Pt/Ta₃N₅ IO thin-film photocatalysts.

CONCLUSIONS

High-quality Ta₂O₅ inverse opal thin films and powders were prepared by the colloidal crystal templating technique. By varying the sizes of the PMMA colloids used to construct the colloidal crystal templates, Ta₂O₅ IO thin films with different macropore diameters and PBGs along the [111] direction in air at 337, 359, 399, 443, 475, 551, 601, and 642 nm were successfully prepared (i.e., spanning from the UV region right across the visible spectrum). A detailed investigation of the optical properties of the Ta₂O₅ IOs was undertaken, with the PBG properties being accurately described by a modified Bragg's law expression. The potential of Ta₂O₅ IO thin films to be used in liquid refractive index sensing was demonstrated, with the [111] PBG position increasing linearly with solvent refractive index in the macropore. Thermal ammonolysis at 700 °C transformed the Ta₂O₅ IO films and powders into Ta₃N₅ IO films and powders, respectively. A 1 wt % Pt/Ta₃N₅ IO photocatalyst delivered a H₂ production rate of 300 μmol g⁻¹ h⁻¹ in 10 vol % methanol under visible-light irradiation, a rate twice that of a traditional 1 wt % Pt/Ta₃N₅ photocatalyst based on a Ta₃N₅ powder. The enhanced activity of the 1 wt % Pt/Ta₃N₅ IO photocatalyst was attributable to its higher specific surface area. Results offer valuable new insights into the potential of Ta₂O₅ IO and Ta₃N₅ IO materials in sensing and photocatalysis, respectively.

ASSOCIATED CONTENT

Supporting Information

The Supporting Information is available free of charge at <https://pubs.acs.org/doi/10.1021/acs.chemmater.3c01903>.

Experimental setups used to synthesize PMMA colloids, PMMA colloidal crystal thin films, and Ta₃N₅ IOs; setup used for photocatalytic H₂ production tests; optical data for PMMA colloidal crystal thin films; photonic band gap structure diagram for a PMMA colloidal crystal in air; and a table comparing the performance of different Pt/Ta₃N₅

photocatalysts for H₂ production via methanol photo-reforming (PDF)

AUTHOR INFORMATION

Corresponding Author

Geoffrey I. N. Waterhouse – School of Chemical Sciences, The University of Auckland, Auckland 1142, New Zealand; The MacDiarmid Institute for Advanced Materials and Nanotechnology, Auckland 1142, New Zealand; The Dodd-Walls Centre for Photonic and Quantum Technologies, Auckland 1142, New Zealand; orcid.org/0000-0002-3296-3093; Phone: 64-9-9237212; Email: g.waterhouse@auckland.ac.nz; Fax: 64-9-373 7422

Authors

Yusong Dong – School of Chemical Sciences, The University of Auckland, Auckland 1142, New Zealand; The MacDiarmid Institute for Advanced Materials and Nanotechnology, Auckland 1142, New Zealand; The Dodd-Walls Centre for Photonic and Quantum Technologies, Auckland 1142, New Zealand

Fujisaka Ai – Department of Applied Chemistry, Graduate School of Science and Technology for Innovation, Tokushima University, Tokushima 770-8506, Japan

Dongxiao Sun-Waterhouse – School of Chemical Sciences, The University of Auckland, Auckland 1142, New Zealand

Kei-ichiro Murai – Department of Applied Chemistry, Graduate School of Science and Technology for Innovation, Tokushima University, Tokushima 770-8506, Japan; Department of Chemical Science and Technology, Graduate School of Advanced Technology and Science, Tokushima University, Tokushima 770-8506, Japan

Toshihiro Moriga – Department of Applied Chemistry, Graduate School of Science and Technology for Innovation, Tokushima University, Tokushima 770-8506, Japan; Department of Chemical Science and Technology, Graduate School of Advanced Technology and Science, Tokushima University, Tokushima 770-8506, Japan; orcid.org/0000-0001-7236-3554

Complete contact information is available at: <https://pubs.acs.org/10.1021/acs.chemmater.3c01903>

Author Contributions

The manuscript was written through contributions of all authors. All authors have approved the submission of this manuscript.

Notes

The authors declare no competing financial interest.

ACKNOWLEDGMENTS

The authors acknowledge funding support from the University of Auckland (doctoral scholarship for Y.D.), the New Zealand Ministry of Business, Innovation and Employment (MBIE, contract C05X2007, Aotearoa: Green Hydrogen Technology Platform), and the Royal Society Te Apārangi (via award of a James Cook Research Fellowship to G.I.N.W.).

REFERENCES

(1) Waterhouse, G. I. N.; Metson, J. B.; Idriss, H.; Sun-Waterhouse, D. Physical and Optical Properties of Inverse Opal CeO₂ Photonic Crystals. *Chem. Mater.* **2008**, *20*, 1183–1190.

- (2) Waterhouse, G. I. N.; Chen, W. T.; Chan, A.; Sun-Waterhouse, D. Achieving Color and Function with Structure: Optical and Catalytic Support Properties of ZrO₂ Inverse Opal Thin Films. *ACS Omega* **2018**, *3*, 9658–9674.
- (3) Waterhouse, G. I. N.; Waterland, M. R. Opal and Inverse Opal Photonic Crystals: Fabrication and Characterization. *Polyhedron* **2007**, *26*, 356–368.
- (4) Nakabayashi, Y.; Nosaka, Y. The pH Dependence of OH Radical Formation in Photo-Electrochemical Water Oxidation with Rutile TiO₂ Single Crystals. *Phys. Chem. Chem. Phys.* **2015**, *17*, 30570–30576.
- (5) Bauer, E.; Mueller, A. H.; Usov, I.; Suvorova, N.; Janicke, M. T.; Waterhouse, G. I. N.; Waterland, M. R.; Jia, Q. X.; Burrell, A. K.; McCleskey, T. M. Chemical Solution Route to Conformal Phosphor Coatings on Nanostructures. *Adv. Mater.* **2008**, *20*, 4704–4707.
- (6) Waterhouse, G. I. N.; Wahab, A. K.; Al-Oufi, M.; Jovic, V.; Anjum, D. H.; Sun-Waterhouse, D.; Llorca, J.; Idriss, H. Hydrogen Production by Tuning the Photonic Band Gap with the Electronic Band Gap of TiO₂. *Sci. Rep.* **2013**, *3*, No. 2849.
- (7) Sharma, M.; Waterhouse, G. I. N.; Loader, S. W.; Garg, S.; Svirskis, D. High Surface Area Polypyrrole Scaffolds for Tunable Drug Delivery. *Int. J. Pharm.* **2013**, *443*, 163–168.
- (8) Seyfoddin, A.; Chan, A.; Chen, W. T.; Rupenthal, I. D.; Waterhouse, G. I. N.; Svirskis, D. Electro-Responsive Macroporous Polypyrrole Scaffolds for Triggered Dexamethasone Delivery. *Eur. J. Pharm. Biopharm.* **2015**, *94*, 419–426.
- (9) Jovic, V.; Idriss, H.; Waterhouse, G. I. N. Slow Photon Amplification of Gas-phase Ethanol Photo-Oxidation in Titania Inverse Opal Photonic Crystals. *Chem. Phys.* **2016**, *479*, 109–121.
- (10) Yasin, M. N.; Brooke, R. K.; Rudd, S.; Chan, A.; Chen, W. T.; Waterhouse, G. I. N.; Evans, D.; Rupenthal, I. D.; Svirskis, D. 3-Dimensionally Ordered Macroporous PEDOT Ion-Exchange Resins Prepared by Vapor Phase Polymerization for Triggered Drug Delivery: Fabrication and Characterization. *Electrochim. Acta* **2018**, *269*, 560–570.
- (11) Ko, Y. L.; Tsai, H. P.; Lin, K. Y.; Chen, Y. C.; Yang, H. Reusable Macroporous Photonic Crystal-Based Ethanol Vapor Detectors by Doctor Blade Coating. *J. Colloid Interface Sci.* **2017**, *487*, 360–369.
- (12) Zhang, Y.; Qiu, W.; Zhao, Y.; Wang, Y.; Bakenov, Z.; Wang, X. Ultra-fine Zinc Oxide Nanocrystals Decorated Three-Dimensional Macroporous Polypyrrole Inverse Opal as Efficient Sulfur Hosts for Lithium/Sulfur Batteries. *Chem. Eng. J.* **2019**, *375*, No. 122055.
- (13) Yan, H.; Blanford, C. F.; Holland, B. T.; Smyrl, W. H.; Stein, A. General Synthesis of Periodic Macroporous Solids by Templated Salt Precipitation and Chemical Conversion. *Chem. Mater.* **2000**, *12*, 1134–1141.
- (14) Jin, L.; Zhao, Y.; Liu, X.; Wang, Y.; Ye, B.; Xie, Z.; Gu, Z. Dual Signal Glucose Reporter Based on Inverse Opal Conducting Hydrogel Films. *Soft Matter* **2012**, *8*, 4911–4917.
- (15) Velev, O. D.; Kaler, E. W. Structured Porous Materials via Colloidal Crystal Templating: From Inorganic Oxides to Metals. *Adv. Mater.* **2000**, *12*, 531–534.
- (16) Eagleton, T. S.; Searson, P. C. Electrochemical Synthesis of 3D Ordered Ferromagnetic Nickel Replicas using Self-Assembled Colloidal Crystal Templates. *Chem. Mater.* **2004**, *16*, 5027–5032.
- (17) *Photonic Band Gap Materials*; Soukoulis, C. M., Ed.; Springer: Dordrecht, 2012.
- (18) Biswas, R.; Sigalas, M. M.; Subramania, G.; Ho, K. M. Photonic Band Gaps in Colloidal Systems. *Phys. Rev. B* **1998**, *57*, No. 3701.
- (19) Vos, W. L.; Driel, H. M. V.; Megens, M.; Koenderink, A. F.; Imhof, A. Experimental Probes of the Optical Properties of Photonic Crystals. In *Photonic Crystals and Light Localization in the 21st Century*; Springer, 2001; pp 191–218.
- (20) Tubio, C. R.; Guitian, F.; Gil, A. Optimal Filling Fraction of Ta₂O₅ Inverse Opals. *Opt. Mater.* **2013**, *36*, 178–181.
- (21) Kaji, T.; Yamada, T.; Ueda, R.; Xu, X.; Otomo, A. Fabrication of Two-dimensional Ta₂O₅ Photonic Crystal Slabs with Ultra-low Background Emission Toward Highly Sensitive Fluorescence Spectroscopy. *Opt. Express* **2011**, *19*, 1422–1440.
- (22) Fairbrother, F. *The Chemistry of Niobium and Tantalum*; Elsevier Publishing Company: New York, 1967; pp 1–28.
- (23) Musikant, S. *Optical Glass Composition. Optical Materials: An Introduction to Selection and Application*; CRC Press, 1985; p 28.
- (24) Fu, Z. W.; Zhou, M. F.; Qin, Q. Z. Temporal and Spatial TaO Emission Generated from UV Laser Ablation of Ta and Ta₂O₅ in Oxygen Ambient. *Appl. Phys. A: Mater. Sci. Process.* **1997**, *65*, 445–449.
- (25) Ohkubo, H.; Ohtera, Y.; Kawakami, S.; Chiba, T. Design and Fabrication of Multichannel Photonic Crystal Wavelength Filters to Suppress Crosstalk of Arrayed Waveguide Grating. *Jpn. J. Appl. Phys.* **2005**, *44*, No. 1534.
- (26) Baumann, K.; Stöferle, T.; Moll, N.; Mahrt, R. F.; Wahlbrink, T.; Bolten, J.; Mollehauser, Moormann, C.; Scherf, U. Organic Mixed-Order Photonic Crystal Lasers with Ultrasmall Footprint. *Appl. Phys. Lett.* **2007**, *91*, No. 171108.
- (27) Wahlbrink, T.; Bolten, J.; Mollenhauer, T.; Kurz, H.; Baumann, K.; Moll, N.; Stöferle, T.; Mahrt, R. F. Fabrication and Characterization of Ta₂O₅ Photonic Feedback Structures. *Microelectron. Eng.* **2008**, *85*, 1425–1428.
- (28) Kao, C. H.; Chen, H.; Chiu, J. S.; Chen, K. S.; Pan, Y. T. Physical and Electrical Characteristics of the High-k Ta₂O₅ (Tantalum Pentoxide) Dielectric Deposited on the Polycrystalline Silicon. *Appl. Phys. Lett.* **2010**, *96*, No. 112901.
- (29) Lin, J.; Masaaki, N.; Tsukune, A.; Yamada, M. Ta₂O₅ Thin Films with Exceptionally High Dielectric Constant. *Appl. Phys. Lett.* **1999**, *74*, 2370–2372.
- (30) Zhu, Y.; Wang, J.; Zhu, X.; Wang, J.; Zhou, L.; Li, J.; Mei, T.; Qian, J.; Wei, L.; Wang, X. Carbon Dot-Based Inverse Opal Hydrogels with Photoluminescence: Dual-Mode Sensing of Solvents and Metal Ions. *Analyst* **2019**, *144*, 5802–5809.
- (31) Xu, Q.; Mahpeykar, S. M.; Burgess, I. B.; Wang, X. Inverse Opal Photonic Crystals as an Optofluidic Platform for Fast Analysis of Hydrocarbon Mixtures. *ACS Appl. Mater. Interfaces* **2018**, *10*, 20120–20127.
- (32) Wang, T.; Yu, Q.; Zhang, S.; Kou, X.; Sun, P.; Lu, G. Rational Design of 3D Inverse Opal Heterogeneous Composite Microspheres as Excellent Visible-Light-Induced NO₂ Sensors at Room Temperature. *Nanoscale* **2018**, *10*, 4841–4851.
- (33) Amrehn, S.; Wu, X.; Wagner, T. Tungsten Oxide Photonic Crystals as Optical Transducer for Gas Sensing. *ACS Sens.* **2018**, *3*, 191–199.
- (34) Zhao, X.; Xue, J.; Mu, Z.; Huang, Y.; Lu, M.; Gu, Z. Gold Nanoparticle Incorporated Inverse Opal Photonic Crystal Capillaries for Optofluidic Surface Enhanced Raman Spectroscopy. *Biosens. Bioelectron.* **2015**, *72*, 268–274.
- (35) Zhang, Y.; Qiu, J.; Gao, M.; Li, P.; Gao, L.; Heng, L.; Zhang, B. Z.; Jiang, L. A Visual Film Sensor Based on Silole-Infiltrated SiO₂ inverse opal photonic crystal for Detecting Organic Vapors. *J. Mater. Chem. C* **2014**, *2*, 8865–8872.
- (36) Yu, Y.; Brandt, S.; Nicolas, N. J.; Aizenberg, J. Colorimetric Ethanol Indicator Based on Instantaneous, Localized Wetting of a Photonic Crystal. *ACS Appl. Mater. Interfaces* **2020**, *12*, 1924–1929.
- (37) Armstrong, E.; O'Dwyer, C. Artificial Opal Photonic Crystals and Inverse Opal Structures-Fundamentals and Applications from Optics to Energy Storage. *J. Mater. Chem. C* **2015**, *3*, 6109–6143.
- (38) Likodimos, V. Photonic Crystal-Assisted Visible Light Activated TiO₂ Photocatalysis. *Appl. Catal., B* **2018**, *230*, 269–303.
- (39) Temerov, F.; Ankudze, B.; Saarinen, J. J. TiO₂ Inverse Opal Structures with Facile Decoration of Precious Metal Nanoparticles for Enhanced Photocatalytic Activity. *Mater. Chem. Phys.* **2020**, *242*, No. 122471.
- (40) Lin, S.; Zhang, N.; Wang, F.; Lei, J.; Zhou, L.; Liu, Y.; Zhang, J. Carbon Vacancy Mediated Incorporation of Ti₃C₂ Quantum Dots in a 3D Inverse Opal g-C₃N₄ Schottky Junction Catalyst for Photocatalytic H₂O₂ Production. *ACS Sustainable Chem. Eng.* **2021**, *9*, 481–488.
- (41) Collins, G.; Lonergan, A.; McNulty, D.; Glynn, C.; Buckley, D.; Hu, C.; O'Dwyer, C. Ordered Macroporous Photonic Crystal Hot Electron Plasmonic Photocatalysts. *ECS Trans.* **2020**, *98*, No. 53.

- (42) Lv, C.; Wang, L.; Liu, X.; Zhao, L.; Lan, X.; Shi, J. An Efficient Inverse Opal (IO)-TiO₂-MoO_{3-x} for Photocatalytic H₂ Evolution and RhB Degradation—the Synergy Effect of IO Structure and Plasmonic MoO_{3-x}. *Appl. Surf. Sci.* **2020**, *527*, No. 146726.
- (43) Tsang, M.-Y.; Pridmore, N. E.; Gillie, L. J.; Chou, Y.-H.; Brydson, R.; Douthwaite, R. E. Enhanced Photocatalytic Hydrogen Generation Using Polymorphic Macroporous TaON. *Adv. Mater.* **2012**, *24*, 3406–3409.
- (44) Zhang, X.; John, S. Enhanced Photocatalysis by Light-Trapping Optimization in Inverse Opals. *J. Mater. Chem. A* **2020**, *8*, 18974–18986.
- (45) Chen, X.; Zhang, Y.; Pang, Y.; Jiang, Q. Facile Synthesis of Nanoporous NiS Film with Inverse Opal Structure as Efficient Counter Electrode for DSSCs. *Materials* **2020**, *13*, No. 4647.
- (46) Zhu, H.; Zhang, Y.; Zhu, J.; Li, Y.; Jiang, S.; Wu, N.; Wei, Y.; Zhou, J.; Song, Y. Crack-Free Hematite Inverse Opal Photo-Anodes for Enhancing Photo-Electrochemical Water Splitting. *J. Mater. Chem. A* **2020**, *8*, 22929–22937.
- (47) Choi, D. S.; Kim, J.; Hollmann, F.; Park, C. B. Solar-Assisted eBiorefinery: Photoelectrochemical Pairing of Oxyfunctionalization and Hydrogenation Reactions. *Angew. Chem.* **2020**, *132*, 16020–16024.
- (48) Nguyen-Phan, T. D.; Wang, C.; Marin, C. M.; Zhou, Y.; Stavitski, E.; Popczun, E. J.; Yu, Y.; Xu, W.; Howard, B. H.; Stuckman, M. Y.; Waluyo, I.; Ohodnicki, P. R.; Kauffman, D. R. Understanding Three-Dimensionally Interconnected Porous Oxide-Derived Copper Electrocatalyst for Selective Carbon Dioxide Reduction. *J. Mater. Chem. A* **2019**, *7*, 27576–27584.
- (49) Böhm, D.; Beetz, M.; Schuster, M.; Peters, K.; Hufnagel, A. G.; Döblinger, M.; Böller, B.; Bein, T.; Fattakhova-Rohlfing, D. Efficient OER Catalyst with Low Ir Volume Density Obtained by Homogeneous Deposition of Iridium Oxide Nanoparticles on Macroporous Antimony-Doped Tin Oxide Support. *Adv. Funct. Mater.* **2020**, *30*, No. 1906670.
- (50) Schroden, R. C.; Al-Daous, M.; Blanford, C. F.; Stein, A. Optical Properties of Inverse Opal Photonic Crystals. *Chem. Mater.* **2002**, *14*, 3305–3315.
- (51) Zhu, Y.; Sun, Z.; Yin, Z.; Song, H.; Xu, W.; Wang, Y.; Zhyang, L.; Zhang, H. Self-Assembly, Highly Modified Spontaneous Emission and Energy Transfer Properties of LaPO₄: Ce³⁺, Tb³⁺ Inverse Opals. *Dalton Trans.* **2013**, *42*, 8049–8057.
- (52) Brunauer, S.; Emmett, P. H.; Teller, E. Adsorption of Gases in Multimolecular Layers. *J. Am. Chem. Soc.* **1938**, *60*, 309–319.
- (53) Barrett, E. P.; Joyner, L. G.; Halenda, P. P. The Determination of Pore Volume and Area Distributions in Porous Substances. I. Computations from Nitrogen Isotherms. *J. Am. Chem. Soc.* **1951**, *73*, 373–380.
- (54) Patterson, A. L. The Scherrer Formula for X-ray Particle Size Determination. *Phys. Rev.* **1939**, *56*, No. 978.
- (55) Johnson, S. G.; Joannopoulos, J. D. Block-Iterative Frequency-Domain Methods for Maxwell's Equations in a Planewave Basis. *Opt. Express* **2001**, *8*, 173–190.
- (56) Gonçalves, R. V.; Wojcieszak, R.; Uberman, P. M.; Teixeira, S. R.; Rossi, L. M. Insights into the Active Surface Species Formed on Ta₂O₅ Nanotubes in the Catalytic Oxidation of CO. *Phys. Chem. Chem. Phys.* **2014**, *16*, 5755–5762.
- (57) Liu, W. S.; Huang, S. H.; Liu, C. F.; Hu, C. W.; Chen, T. Y.; Perng, T. P. Nitrogen Doping in Ta₂O₅ and its Implication for Photocatalytic H₂ Production. *Appl. Surf. Sci.* **2018**, *459*, 477–482.
- (58) Wang, W.; Fang, H. B.; Zheng, Y. Z.; Che, Y.; Tao, X.; Chen, J. F. In situ Template-Free Synthesis of a Novel 3D p-n Heteroarchitecture Ag₃PO₄/Ta₃N₅ Photocatalyst with High Activity and Stability under Visible Radiation. *RSC Adv.* **2015**, *5*, 62519–62526.
- (59) Li, Y.; Feng, Q.; Wang, H.; Zhou, G.; Wang, Z. S. Reduced Graphene Oxide-Ta₃N₅ Composite: a Potential Cathode for Efficient Co(bpy)₃^{3+/2+} Mediated Dye-Sensitized Solar Cells. *J. Mater. Chem. A* **2013**, *1*, 6342–6349.
- (60) Chun, W. J.; Ishikawa, A.; Fujisawa, H.; Takata, T.; Kondo, J. N.; Hara, M.; Kawai, M.; Matsumoto, Y.; Domen, K. Conduction and Valence Band Positions of Ta₂O₅, TaON, and Ta₃N₅ by UPS and Electrochemical Methods. *J. Phys. Chem. B* **2003**, *107*, 1798–1803.
- (61) Fu, J.; Wang, F.; Xiao, Y.; Yao, Y.; Feng, C.; Chang, L.; Jiang, C.-H.; Kunzelmann, V. F.; Wang, Z. M.; Govorov, A. O.; Sharp, I. D.; Li, Y. Identifying Performance-Limiting Deep Traps in Ta₃N₅ for Solar Water Splitting. *ACS Catal.* **2020**, *10*, 10316–10324.
- (62) Tabata, M.; Maeda, K.; Higashi, M.; Lu, D.; Takata, T.; Abe, R.; Domen, K. Modified Ta₃N₅ Powder as a Photocatalyst for O₂ Evolution in a two-step Water Splitting System with an Iodate/Iodide Shuttle Redox Mediator under Visible Light. *Langmuir* **2010**, *26*, 9161–9165.
- (63) Li, W.; Sun, Z.; Tian, D.; Nevirkovets, I. P.; Dou, S. X. Platinum Dendritic Nanoparticles with Magnetic Behavior. *J. Appl. Phys.* **2014**, *116*, No. 033911.
- (64) Dang, H. X.; Lin, Y. M.; Klavetter, K. C.; Cell, T. H.; Heller, A.; Mullins, C. B. Lithium Insertion/Deinsertion Characteristics of Nanostructured Amorphous Tantalum Oxide Thin Films. *ChemElectroChem* **2014**, *1*, 158–164.
- (65) Purvis, K. L.; Lu, G.; Schwartz, J.; Bernasek, S. L. Surface Characterization and Modification of Indium Tin Oxide in Ultrahigh Vacuum. *J. Am. Chem. Soc.* **2000**, *122*, 1808–1809.
- (66) Khan, S.; Santos, M. J.; Malfatti, C. F.; Dupont, J.; Teixeira, S. R. Pristine Ta₃N₅ Nanotubes: Trap-Driven High External Biasing Perspective in Semiconductor/Electrolyte Interfaces. *Chem. - Eur. J.* **2016**, *22*, 18501–18511.
- (67) Hara, M.; Hitoki, G.; Takata, T.; Kondo, J. N.; Kobayashi, H.; Domen, K. TaON and Ta₃N₅ as New Visible Light Driven Photocatalysts. *Catal. Today* **2003**, *78*, 555–560.
- (68) Feng, W.; Chen, G.; Li, L.; Lv, G.; Zhang, X.; Niu, E.; Liu, C.; Yang, S. Z. Characteristics of (Ti, Ta) N Thin Films Prepared by Using Pulsed High Energy Density Plasma. *J. Phys. D: Appl. Phys.* **2007**, *40*, 4228.
- (69) Maeda, K.; Nishimura, N.; Domen, K. A Precursor Route to Prepare Tantalum (V) Nitride Nanoparticles with Enhanced Photocatalytic Activity for Hydrogen Evolution under Visible Light. *Appl. Catal., A* **2009**, *370*, 88–92.
- (70) Dabirian, A.; Van de Krol, R. Resonant Optical Absorption and Defect Control in Ta₃N₅ Photoanodes. *Appl. Phys. Lett.* **2013**, *102*, No. 033905.
- (71) Vinayan, B. P.; Ramaprabhu, S. Platinum-TM (TM = Fe, Co) Alloy Nanoparticles Dispersed Nitrogen Doped (Reduced Graphene Oxide-Multiwalled Carbon Nanotube) Hybrid Structure Cathode Electrocatalysts for High Performance PEMFC Applications. *Nanoscale* **2013**, *5*, 5109–5118.
- (72) Guo, Q.; Zhao, J.; Yang, Y.; Huang, J.; Tang, Y.; Zhang, X.; Li, Z.; Yu, X.; Shen, J.; Zhao, J. Mesocrystalline Ta₃N₅ Superstructures with long-lived charges for Improved Visible Light Photocatalytic Hydrogen Production. *J. Colloid Interface Sci.* **2020**, *560*, 359–368.
- (73) Cui, J.; Qi, Y.; Dong, B.; Mu, L.; Ding, Q.; Liu, G.; Jia, M.; Zhang, F.; Li, C. One-Pot Synthesis of BaMg_{1/3}Ta_{2/3}O_{3-x}Ny/Ta₃N₅ Heterostructures as H₂-Evolving Photocatalysts for Construction of Visible-Light-Driven Z-scheme Overall Water Splitting. *Appl. Catal., B* **2019**, *241*, 1–7.
- (74) Pei, L.; Wang, H.; Wang, X.; Xu, Z.; Yan, S.; Zou, Z. Nanostructured TaON/Ta₃N₅ as a Highly Efficient Type-II Heterojunction Photoanode for Photoelectrochemical Water Splitting. *Dalton Trans.* **2018**, *47*, 8949–8955.
- (75) Bian, Z.; Tachikawa, T.; Majima, T. Superstructure of TiO₂ Crystalline Nanoparticles Yields Effective Conduction Pathways for Photogenerated Charges. *J. Phys. Chem. Lett.* **2012**, *3*, 1422–1427.
- (76) Ye, J.; Liu, W.; Cai, J.; Chen, S.; Zhao, X.; Zhou, H.; Qi, L. Nanoporous Anatase TiO₂ Mesocrystals: Additive-Free Synthesis, Remarkable Crystalline-Phase Stability, and Improved Lithium Insertion Behavior. *J. Am. Chem. Soc.* **2011**, *133*, 933–940.
- (77) Zhu, Y.; Wan, T.; Wen, X.; Chu, D.; Jiang, Y. Tunable Type I and II Heterojunction of CoO_x Nanoparticles Confined in g-C₃N₄ Nanotubes for Photocatalytic Hydrogen Production. *Appl. Catal., B* **2019**, *244*, 814–822.
- (78) Zhao, H.; Li, G.; Tian, F.; Jia, Q.; Liu, Y.; Chen, R. g-C₃N₄ Surface-Decorated Bi₂O₂CO₃ for Improved Photocatalytic Perform-

ance: Theoretical Calculation And Photodegradation Of Antibiotics in Actual Water matrix. *Chem. Eng. J.* **2019**, 366, 468–479.

(79) Al-Azri, Z. H. N.; AlOufi, M.; Chan, A.; Waterhouse, G. I. N.; Idriss, H. Metal Particle Size Effects on the Photocatalytic Hydrogen Ion Reduction. *ACS Catal.* **2019**, 9, 3946–3958.

(80) Chen, S.; Qi, Y.; Ding, Q.; Li, Z.; Cui, J.; Zhang, F.; Li, C. Magnesia Interface Nanolayer Modification of Pt/Ta₃N₅ for Promoted Photocatalytic Hydrogen Production under Visible Light Irradiation. *J. Catal.* **2016**, 339, 77–83.

(81) Liu, X.; Zhao, L.; Domen, K.; Takanabe, K. Photocatalytic Hydrogen Production Using Visible-Light-Responsive Ta₃N₅ Photocatalyst Supported on Monodisperse Spherical SiO₂ Particulates. *Mater. Res. Bull.* **2014**, 49, 58–65.

(82) Hisatomi, T.; Otani, M.; Nakajima, K.; Teramura, K.; Kako, Y.; Lu, D.; Domen, K.; et al. Preparation of Crystallized Mesoporous Ta₃N₅ Assisted by Chemical Vapor Deposition of Tetramethyl Orthosilicate. *Chem. Mater.* **2010**, 22, 3854–3861.

(83) Cui, J.; Liu, T.; Dong, B.; Qi, Y.; Yuan, H.; Gao, J.; Yang, D.; Zhang, F. Flux-Assisted Synthesis of Prism-Like Octahedral Ta₃N₅ Single-Crystals with Controllable Facets for Promoted Photocatalytic H₂ Evolution. *Sol. RRL* **2021**, 5, No. 2000574.

(84) Kishida, K.; Watanabe, T. Improvement of Photocatalytic Activity of Tantalum Nitride by Ammonothermal Treatment at High Pressure. *J. Solid State Chem.* **2012**, 191, 15–18.

(85) Eftekhari, E.; Broisson, P.; Aravindakshan, N.; Wu, Z.; Cole, I. S.; Li, X.; Zhao, D.; Li, Q. Sandwich-Structured TiO₂ Inverse Opal Circulates Slow Photons for Tremendous Improvement in Solar Energy Conversion Efficiency. *J. Mater. Chem. A* **2017**, 5, 12803–12810.

(86) Liu, J.; Jin, J.; Li, Y.; Huang, H. W.; Wang, C.; Wu, M.; Chen, L.-H.; Su, B. Tracing the Slow Photon Effect in a ZnO Inverse Opal Film for Photocatalytic Activity Enhancement. *J. Mater. Chem. A* **2014**, 2, 5051–5059.

(87) Wu, M.; Jin, J.; Liu, J.; Deng, Z.; Li, Y.; Deparis, O.; Su, B. High Photocatalytic Activity Enhancement of Titania Inverse Opal Films by Slow Photon Effect Induced Strong Light Absorption. *J. Mater. Chem. A* **2013**, 1, 15491–15500.

(88) Raja-Mogan, T.; Lehoux, A.; Takashima, M.; Kowalska, E.; Ohtani, B. Slow Photon-Induced Enhancement of Photocatalytic Activity of Gold Nanoparticle-Incorporated Titania Inverse Opal. *Chem. Lett.* **2021**, 50, 711–713.